CZECH TECHNICAL UNIVERSITY IN PRAGUE

Faculty of Nuclear Sciences and Physical Engineering

Department of Physics

Diploma Thesis

Exclusive production of Rho in p-Pb Ultra-Peripheral Collisions

Bc. David Horák

Supervisor: Guillermo Contreras, Ph.D.

Prague, 2015

ČESKÉ VYSOKÉ UČENÍ TECHNICKÉ
V PRAZE
Fakulta jaderná a fyzikálně inženýrská
Katedra fyziky

Diplomová práce

Exkluzivní produkce Rho v ultra-periferálních srážkách p-Pb

Bc. David Horák

Vedoucí práce: Guillermo Contreras, Ph.D.

Praha, 2015

Prohlášení:

Prohlašuji, že jsem svou diplomovou práci vypracoval samostatně a použil jsem pouze podklady (literaturu, software, atd.) uvedené v přiloženém seznamu.

Nemám závažný důvod proti užití tohoto školního díla ve smyslu § 60 Zákona č.121/2000 Sb., o právu autorském, o právech souvisejících s právem autorským a o změně některých zákonů (autorský zákon).

V Praze dne ....

David Horák

Acknowledgement

I would like to express my gratitute to my supervisor, Guillermo Contreras, Ph.D. for his willingness, patience, professional feedback and language corrections. I would also like to thank to Ing. Jaroslav Adam for technical support and helpful consultations and to Mgr. Michal Broz, Ph.D for preparation of the data sample. Last but not least, please allow me to thank to my family, my friends and to all who supported me during the creation of this work.

Abstract: The LHC is not only the most powerful collider for proton-proton and heavy ion collisions, but it is also the most powerful source of photon collisions. The accelerated protons and ions carry an electromagnetic field, which can be viewed as photons. The photon-photon and photon-proton (or ion) processes can be studied in ultra-peripheral collisions (UPC). These processes offer an unique opportunity to study fundamental interactions in QED and QCD. This thesis presents a preliminary study for the first measurement of the cross section for exclusive rho protoproduction in UPC p-Pb collisions at mid rapidity with the ALICE detector at the LHC.

Key words: Ultra-peripheral collisions, photoproduction, rho meson, ALICE.

Abstrakt: LHC není jen nejsilnějším srážečem protonů s protony a těžkých iontů, ale také nejsilnějším zdrojem srážek fotonů. Urychlené protony a ionty jsou doprovázeny elektromagnetickým polem, které se chová jako fotony. Foton-fotonové a foton-protonové procesy mohou být studovány v ultra-periferálních srážkách (UPC). Tyto procesy poskytují unikátní příležitost studia fundamentálních interakcí v QED a QCD. Tato práce prezentuje předběžné výsledky měření účinného průřezu exkluzivní fotoprodukce rho mezonu v ultra-periferálních srážkách p-Pb ve střední rapiditě na ALICE detektoru na LHC.

Klíčová slova: Ultra-periferální srážky, fotoprodukce, rho mezon, ALICE.

Contents

List of Figures

Preface

The LHC is not only the most powerful collider for proton-proton and heavy ion collisions, but it is also the most powerful source of photon collisions. The accelerated protons and ions carry an electromagnetic field, which can be viewed as photons. The photon-photon and photon-proton (or ion) processes can be studied in ultra-peripheral collisions (UPC). These processes offer an unique opportunity to study fundamental interactions in QED and QCD.

The purpose of this thesis is to compute the preliminary cross section for exclusive photoproduction of a ρ^0 meson in ultra-peripheral p-Pb collisions. This process was never measured at the LHC before. The preliminary cross section will be compared to the result from HERA accelerator at the same centre-of-mass energy. However, the LHC can offer measurement of the cross section at the centre-of-mass energies larger than that at HERA. The techniques developed in this work will be applied to perform these measurements at the new energies.

The first chapter is dedicated to the introduction of terms and variables used in this work. The production of particles in ultra-peripheral collisions is explained, concentrating on the photoproduction of a ρ^0 meson, which is studied in this work.

In the second chapter the ALICE detector at LHC is presented. I am focusing primarily on description of detectors important for my work. Then the trigger system and data acquisition system of ALICE is described. The end of the chapter is dedicated to the data processing and tools used for the reconstruction and analysis.

The third chapter presents measurement results of the ρ^0 meson cross section at HERA accelerator. Moreover, the measurement of the ρ^0 meson cross section in Pb-Pb UPC at ALICE is described. This analysis is very similar to my work and therefore it is described in more detail.

In the last chapter I will present my analysis of exclusive photoproduction of the ρ^0 meson in ultra-peripheral p-Pb collisions. I will describe the data I am using. Then a quality assurance of data is shown. The chapter continues with information about computing luminosity, selection criteria and the difficulties in background subtraction. After that the Monte Carlo data, which are used for estimation of efficiency and acceptance of the detector, are described. Finally the computed preliminary cross section of ρ^0 is presented and it is compared to the HERA results.

Chapter 1

Introduction to UPC

This chapter is dedicated to the introduction of terms and variables used in this work. A collision of particles is defined as well as centrality of collision and its relationship to ultra-peripheral collisions. After that the production of particles in ultra-peripheral collisions is explained, concentrating on the photoproduction of a ρ^0 meson, which is studied in this work.

1.1 Definitions

1.1.1 Coordinate system

The coordinate system used in high-energy particle physics can be seen in Figure 1.1. The center of coordinate system is in the interaction point (IP). The z-axis is parallel to the beam and it is called the longitudinal direction. The perpendicular x and y axis form the transverse direction, in which the azimuthal angle φ is defined. The deviation from the z-axis is called the polar angle θ.

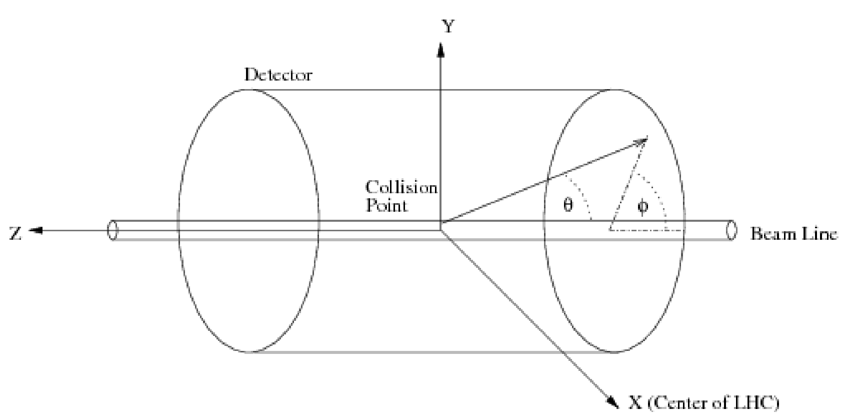

Figure 1.1: Coordinate system at the LHC. Taken from [1].

1.1.2 Cross section

The cross section is the basic quantity in particle physics. It expresses the probability of a particular event. Moreover, the differential cross section $\frac{\mathrm{d}\sigma}{\mathrm{d}\Omega}$ gives us information about the interaction or about the interacting particles. The total cross section σ_{tot} is defined as the integral over the whole solid angle ($\mathrm{d}\Omega = \sin(\theta)\,\mathrm{d}\theta\mathrm{d}\varphi$):

$$\sigma_{tot} = \oint \frac{\mathrm{d}\sigma}{\mathrm{d}\Omega}\mathrm{d}\Omega. \tag{1.1}$$

The unit of the cross section is m^2, but in particle physics it is common to use units of barn. A barn b is defined as $10^{-28}\mathrm{m}^2$ and is approximately the cross section-area of an uranium nucleus.

1.1.3 Luminosity

The event rate R is proportional to the interaction cross section σ and the factor of proportionality is called the luminosity L:

$$R = \sigma L. \tag{1.2}$$

The dimensions of luminosity are events per time per area, usually expressed in units $\mathrm{cm}^{-2}\mathrm{s}^{-1}$ or $\mathrm{b}^{-1}\mathrm{s}^{-1}$. In the circular accelerator with bunches containing n_1 and n_2 particles the luminosity can be written as:

$$L = f\frac{n_1 n_2}{4\pi\sigma_x\sigma_y}, \tag{1.3}$$

where f is the frequency of bunch collisions and σ_x, σ_y are Gaussian profiles of the beam.

The amount of recorded data in experiment can be represented by the integrated luminosity, which is the integral of luminosity over the time period:

$$L_{int} = \int L\mathrm{d}t. \tag{1.4}$$

1.1.4 Rapidity and pseudorapidity

To describe of the velocity of particles it is useful to define the rapidity y:

$$y = \frac{1}{2}\ln\frac{E + p_L}{E - p_L}. \tag{1.5}$$

This variable is not a Lorentz-invariant, but it is additive in Lorentz transformations along the z-axis, similarly to the velocity in Galilean transformation.

The pseudorapidity is defined as:

$$\eta = \frac{1}{2}\ln\frac{|\overrightarrow{p}| + p_L}{|\overrightarrow{p}| - p_L} = -\ln\tan\frac{\theta}{2}. \tag{1.6}$$

As can be seen the pseudorapidity depends only on polar angle and therefore can be easily measured in a detector. Some values of pseudorapidity for different azimuthal angles can be seen in Figure 1.2.

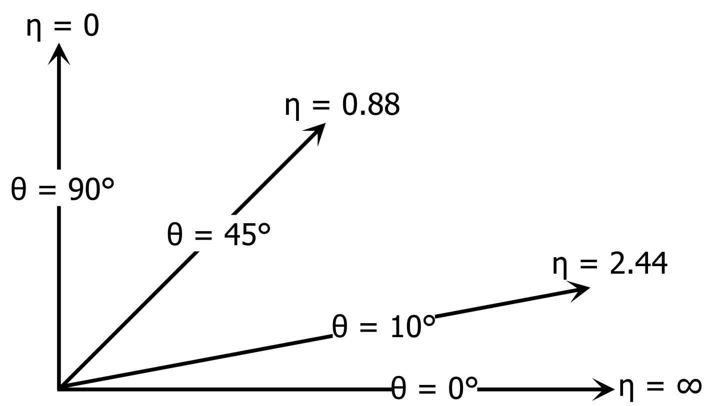

Figure 1.2: Pseudorapidity values for different θ angles.

1.1.5 Impact parameter, centrality, multiplicity

A collision of particles is characterized by a centrality (see Figure 1.3), which is closely connected to an impact parameter b . This parameter is defined as the perpendicular distance between the path of two particles with a radius R_1 and R_2 . If the impact parameter is close to 0, the nuclei hit head on and we call it central collision. As the impact parameter increases, the centrality of collision decreases to peripheral collisions ($b \sim R_1 + R_2$). If the impact parameter is larger than the sum of nuclear radii, an ultra-peripheral collision (UPC) may occur.

Although the centrality of the collision can not be directly measured, it is possible to determine the centrality indirectly. The centrality of collision influences the number of produced particles in the collision. This is called the multiplicity.

1.2 Ultra-peripheral collisions

The pancake shape of the nuclei at the ultra-relativistic velocities is due to the Lorentz contraction in the direction of movement. In 1924, Enrico Fermi showed that the moving electromagnetic fields of a charged particle are equivalent to the flux of virtual photons [8]. The electromagnetic field of nuclei is contracted and its intensity (and the number of photons surroundings the nucleus) is proportional to Z^2 .

In ultra-peripheral collisions the strong interaction is suppressed due to the short range and only electromagnetic processes occur.

1.2.1 Photoproduction

Photoproduction is an electromagnetic process, in which some particles are produced. For example two photons collide and produce lepton-antilepton pair.

In photonuclear interaction a photon interacts with one of the nucleus. This interaction can be coherent, if the photon interacts with the whole nucleus, or incoherent

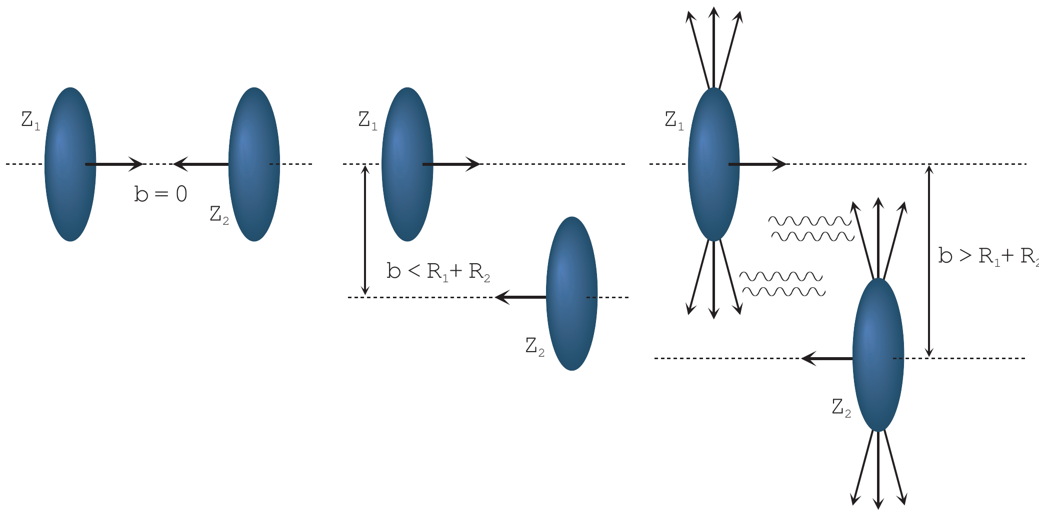

Figure 1.3: Centrality of a collision. From left: central collision, peripheral collision, ultra-periferal collision.

depending on the wavelength of the virtual photon. The cross section of vector meson photoproduction in Pb-Pb UPCs can be expressed as:

$$\frac{d\sigma_{PbPb}(y)}{dy} = N_{\gamma/Pb}(y,M)\,\sigma_{\gamma Pb}(y) + N_{\gamma/Pb}(-y,M)\,\sigma_{\gamma Pb}(-y)\,, \tag{1.7}$$

where M is the mass of the produced vector meson, y is its rapidity, $\sigma_{\gamma Pb}(y)$ is the photoproduction cross section and $N_{\gamma/Pb}$ is the photon flux. There are two terms because each of the nuclei can act as the source of photon [9].

Similar formula can be written for p-Pb collisions:

$$\frac{d\sigma_{pPb}(y)}{dy} = N_{\gamma/Pb}(y,M)\,\sigma_{\gamma p}(y)\,. \tag{1.8}$$

There is only one term because the probability of photon emission by proton is very small. The photoproduction in p-Pb collisions can be elastic or dissociative. In the former, proton remain in its ground state, in the latter case proton breaks up.

The photon flux per unit area is given by:

$$n(k,b) = \frac{\alpha Z^2}{\pi^2 b^2} x^2 \left[K_1^2(x) + \frac{1}{\gamma} K_0^2(x)\right], \tag{1.9}$$

where k is the photon energy in the nucleus frame, K_0 and K_1 are Bessel functions and $x = \frac{kb}{\gamma}$. The photon flux of a lead nucleus can be obtained using corresponding values in:

$$N_{\gamma/Pb}(y,M) = k\frac{dn(k)}{dk}. \tag{1.10}$$

According to a Vector meson dominance model (VMD) [10], which describes interaction between energetic photons and hadronic matter, the cross section for producing

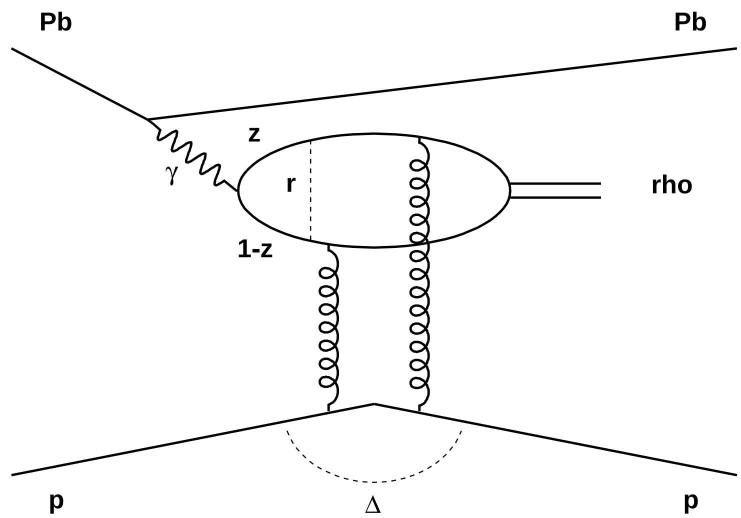

Figure 1.4: Rho production diagram in the Color dipole model.

a vector meson, such as ρ^0, ω, ϕ or J/ψ, grows with energy and it is very large at LHC energies.

There are several models based on Equation 1.7 that predict cross section for photonuclear production. In this work we used model by Klein and Nystrand, which is implemented in the STARLIGHT [11] Monte Carlo program. This model is based on the Vector dominance model.

1.2.2 Rho meson photoproduction in p-Pb

The $\rho(770)^0$ belongs to light unflavored vector mesons ($J^{PC} = 1^{--}$) with quark content $\frac{1}{\sqrt{2}}\left(u\bar{u} - d\bar{d}\right)$. Its mass is (775.26 ± 0.25) MeV and it has a full width (149.1 ± 0.8) MeV. The mean lifetime is 4.5×10^{-24} s and it decays dominantly into $\pi^+\pi^-$ pair. The leptonic and four-pion decay are suppressed and occur with a branching ratio of about 10^{-5} [12].

In this work the photoproduction of ρ^0 in p-Pb UPC is studied. Because the intensity of electromagnetic field is proportional to Z^2, in p-Pb collisions, the lead is the source of photon and the proton is the target. Photon-photon and photon-lead interactions are suppressed.

The production diagram of the rho meson in the Color dipole model can be seen in Figure 1.4. The photon interacts with a proton and produce a ρ^0 meson. This interaction can be elastic if the proton continue or dissociative if proton breaks up.

1.2.3 Rho event in the detector

Most of the UPC triggers are based on the low multiplicity events in ALICE. In these ultra-peripheral collisions only one or two particles are produced. It means that the activity in the detector is very low and only few tracks are present. However, in UPC

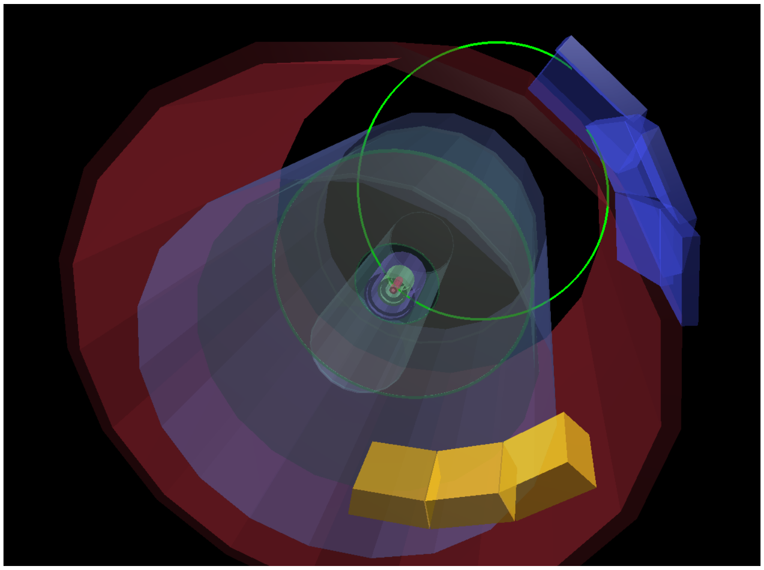

Figure 1.5: An UPC event in ALICE detector.

also a multitracks events from jet production can be present. These events are not catched by the UPC triggers.

The transverse momentum of products in UPC depends on size of the target and originates from the uncertainty principle. In the coherent production on lead the transverse momentum is below 150 MeV/c. In the elastic production on proton the transversal momentum is below 1 GeV. Thanks to the low magnetic field, the ALICE detector is ideal for studying these processes.

In Figure 1.5 can be seen a good candidate for a ρ^0 meson. Only two good reconstructed tracks identified as pions are visible.

Chapter 2

ALICE Detector at CERN

In this chapter the ALICE (A Large Ion Collider Experiment) detector at LHC is presented. I am focusing on description of detectors used in my analysis. Then the trigger system and data acquisition (DAQ) system of ALICE is described. The end of the chapter is dedicated to the data processing and tools used to the reconstruction and analysis.

2.1 CERN

The European Organization for Nuclear Research (CERN) was establish in 1954. It is situated on the Franco-Swiss border near Geneva. Today it has 21 member states, most of which are European countries. Some countries have an observer status which means that they can attend council meeting, receive council documents, but they have no decision rights. These countries include the USA, India, Japan, the Russian Federation, Turkey. UNESCO and the European Commission are also listed among the observers. There are also many non-members states.

Main interests of CERN lie in basic research. Scientists from all over the world try to find answers to such questions as: "What is the universe made of? How did it start?" [13]. To achieve this, CERN is also heavily involved in development of new technologies, worldwide scientific cooperation and education of scientists.

Several discoveries made at CERN resulted in Nobel Prize awards. The most important results of CERN include discovery of neutral currents, of W and Z bosons, number of neutrino families at LEP, first creation of antihydrogen atoms and of Higgs boson with mass around 125 GeV. Moreover, many new technologies were invented at CERN, e.g. World Wide Web.

2.2 Large Hadron Collider

After discovery of W and Z bosons at SppS, there was a desire to discover the last particle of the Standard Model - the Higgs boson. The Large Hadron Collider (LHC) was build in the old LEP tunnel in the depth of around 100 meters underground. The length of the tunnel is 27 km. The collider consists of 1232 superconducting dipole magnets 15 meters in length, which bend the beams, and 392 quadrupole magnets,

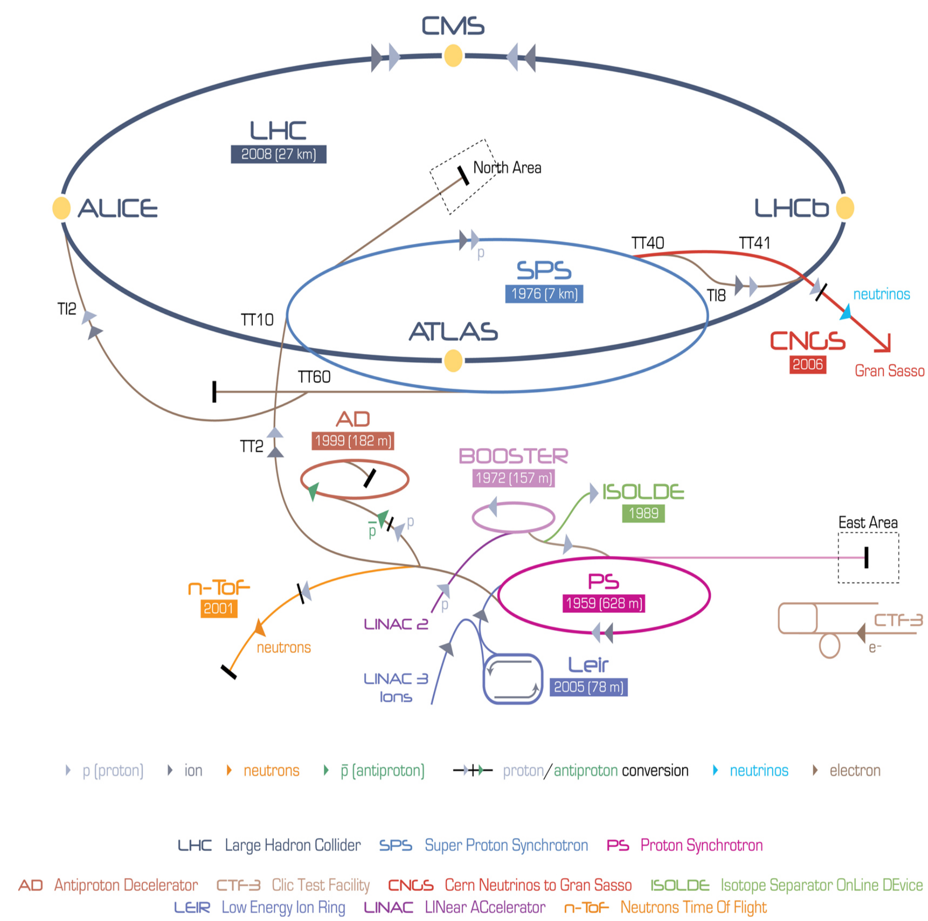

Figure 2.1: CERN accelerator complex. Taken from [2].

which focus the beams. The magnetic field in the dipole magnets is 8 T. The use of superconducting magnets presents a big advantage as they consume less power. The two beams travel in opposite directions in separate beam pipes, in which the ultrahigh vacuum (up to $10^{-11}\ mbar$) is required. The vacuum system of LHC is the largest in the world, its volume is 15,000 cubic meters, more than the nave of any cathedral [13].

The protons (or ions) must be preaccelerated before they are injected into the LHC. The CERN accelerator complex can be seen in Figure 2.1. The source of protons is hydrogen gas. An electric field strips hydrogen atoms of their electrons to produce protons. Linac 2 accelerates the protons to an energy of 50 MeV. The beam is then injected into the Proton Synchrotron Booster (PSB), which accelerates the protons to 1.4 GeV, followed by the Proton Synchrotron (PS), which boosts the beam to 25 GeV. Protons are then sent to the Super Proton Synchrotron (SPS) where they are accelerated to 450 GeV. The protons injected into the LHC at 450 GeV are boosted by 16 radiofrequency cavities up to 4 TeV. The top energy is reached in 15 minutes.

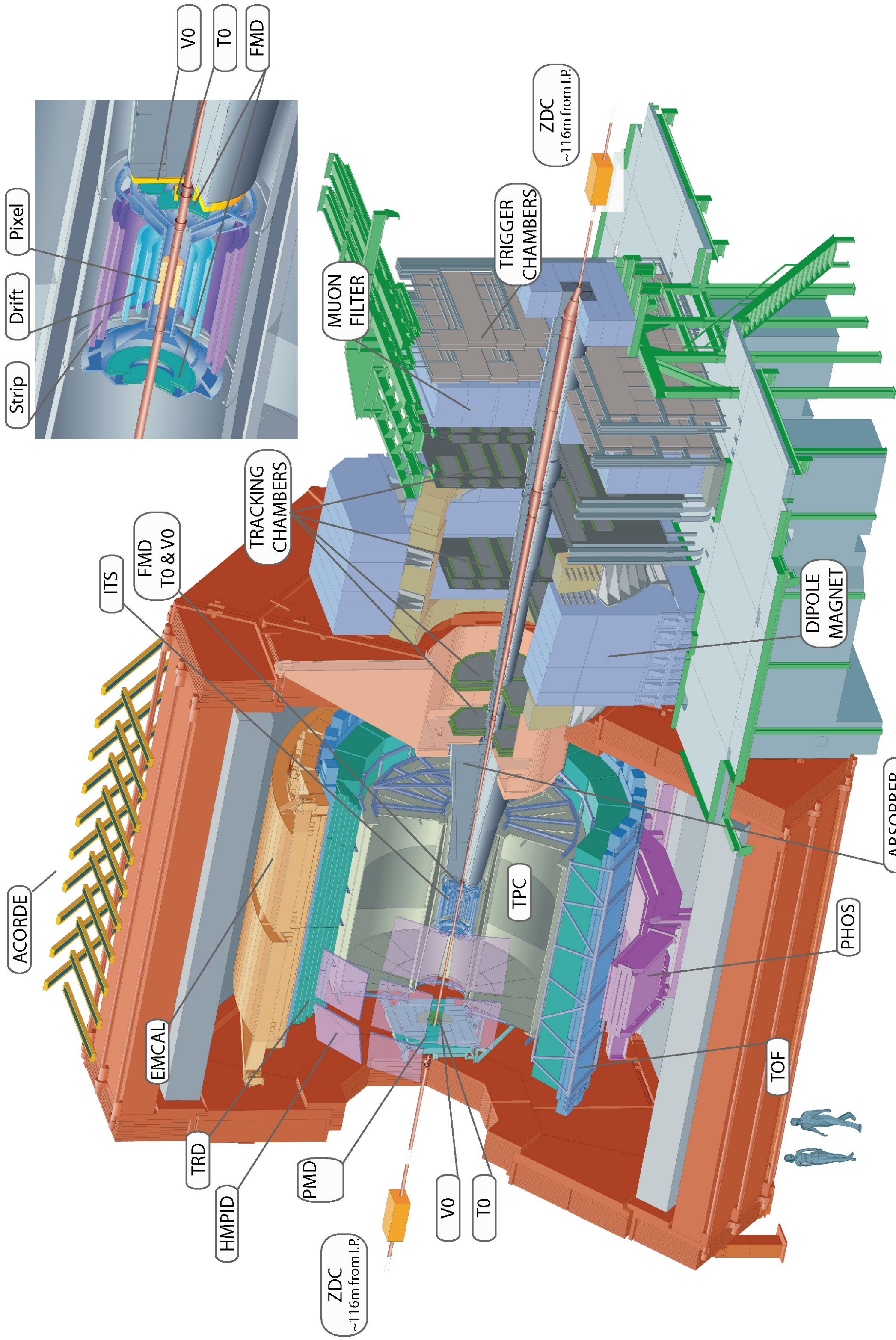

Figure 2.2: A schematic layout of the ALICE detector. Taken from [3].

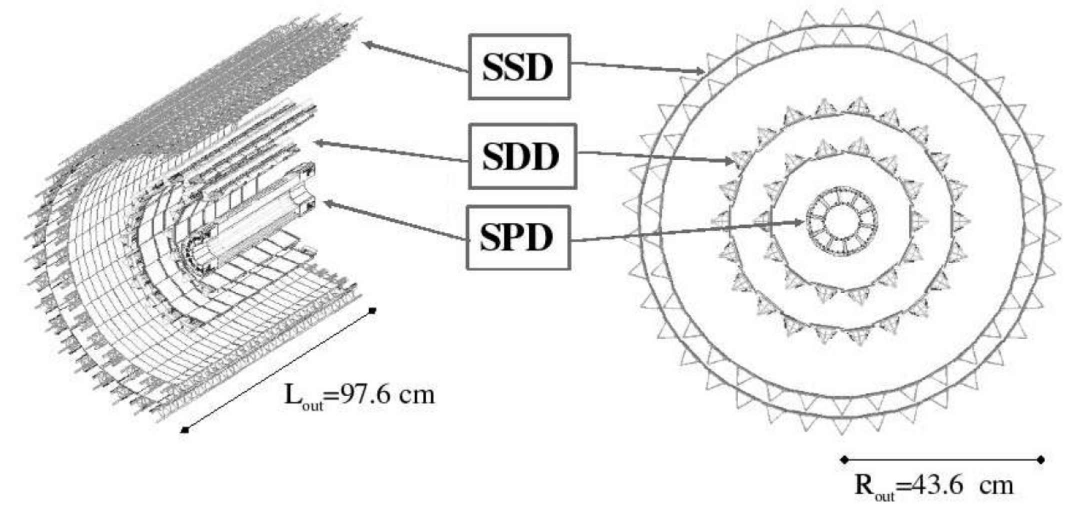

Figure 2.3: Layout of the ITS. Taken from [3].

Lead ions start from vaporized lead and enter Linac3. After that they are accelerated in the Low Energy Ion Ring (LEIR) and then they are injected into PS and follow the same route as the protons.

When the top energy is reached, collisions can start at four intersection points. It is the place of the four main experiments - ATLAS, ALICE, CMS and LHCb.

2.3 ALICE experiment

ALICE detector was designed to study quark-gluon plasma in nucleus-nucleus collision. The lead collisions are the main physics programme, but proton-nucleus and proton-proton programme is present too. In addition, ALICE is also excellent detector for studying UPC. The ALICE experiment is located 56 m below ground and its dimensions are $16 \times 16 \times 26\,\mathrm{m}^3$ with a total weight of approximately 10000 t and a magnetic field of B=0.5 T.

The ALICE detector, which can be seen in Figure 2.2, consist of the central barrel part and a Forward Muon Spectrometer. The central part is embedded in a large solenoid magnet, which was used in the L3 experiment at LEP. In 2013 the ALICE experiment consisted of 18 different detectors. The barrel contains the Inner Tracking System (ITS), Time-Projection Chamber (TPC), Time-of-Flight (TOF), Transition Radiation Detector (TRD), two electromagnetic calorimeters (Photon Spectrometer PHOS and Electro-Magnetic Calorimeter EMCal) and High Momentum Particle Identification Detector (HMPID). Several smaller forward detectors (T0, V0, PMD, FMD and ZDC) are placed at small angles along the Beam Pipe. An array of scintillators (ACORDE) is located on top of the magnet, which is used to trigger on cosmic rays.

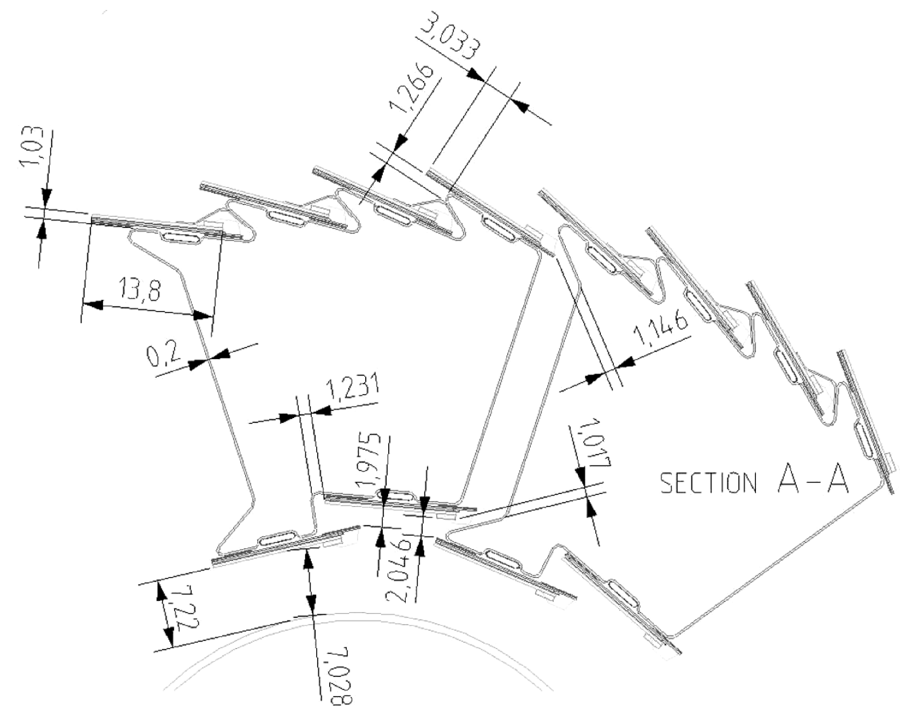

Figure 2.4: A schematic of the SPD. Taken from [3].

2.3.1 ITS

The Inner Tracking System (ITS) is the central detector closest to the beam pipe. The main task of ITS is to localize the primary vertex. The resolution is better then 100 μm, so it is possible to reconstruct the secondary vertices from decays of hyperons and D and B mesons. Other tasks are to identify particles with momentum below 200 MeV/c and reconstruction of particles passing the dead regions of the TPC.

The ITS consists of 6 cylindrical layers of silicon detectors. Its layout can be seen in Figure 2.3. Layer radius varies from 4 to 43 cm and the detector covers the pseudo-rapidity range of $|\eta| < 0.9$. The inner two layers consist of Silicon Pixel Detectors (SPD), the following two are equipped by Silicon Drift Detectors (SDD) and the outer are formed by double-sided Silicon Strip Detectors (SSD). The four outer layers have analog readout, therefore they can be used for particle identification (PID).

Silicon Pixel Detector

The Silicon Pixel Detector (SPD) consists of two layers. Because the track density could be as high as 50 tracks/cm^2, it is based on hybrid silicon pixels. There is also very high radiation level, which could reach $2,7$ kGy in 10 years of operation [3]. The SPD is the key to the determination of the primary and secondary vertex position from the weak decays of strange, charm and beauty particles.

The basic detector module is the half-stave, each consisting of two ladders, one Multi-Chip Module and one multi-layer interconnect. The ladder consists of two-dimensional sensor matrix formed by 256×160 pixel cells. The dimensions of sensor

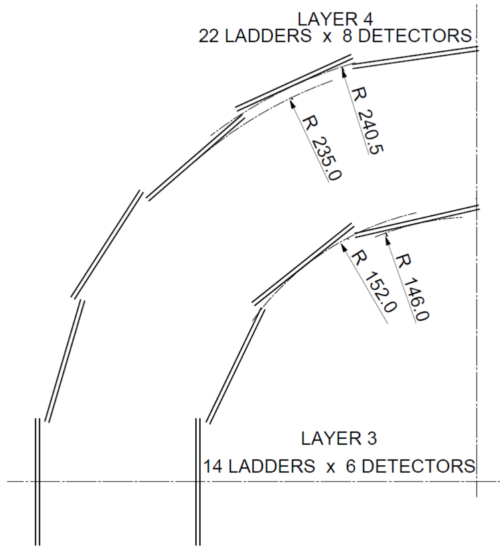

Figure 2.5: SDD ladders layout. Taken from [3].

cells are 50 μm $\times$ 425 μm. The thickness of the sensor is 200 μm and it is bumb-bonded to the readout chip.

The readout is binary - signal above threshold is represented by logical 1. Each pixel also provides a Fast-OR digital pulse, which is used for self-triggering and for the L0-trigger decision. After reception of the L1 trigger signal, data from pixels are stored in multi-event buffers. If the L2 trigger signal arrives, the data are processed by Multi-Chip Module and are sent by optical cables to the control room, where the read-out electronics are located.

The SPD is supported by a carbon-fibre support as is shown at Figure 2.4. This support is divided into 10 identical parts and provides a very high stiffness. The precise position of each pixel is very important and this support is durable to any deformations. The power dissipated in the front-end chips is more than 1 kW [3]. The carbon-fibre support provides the necessary thermal contact between the chips and the cooling system, which is based on evaporative system with C_4F_{10} as coolant.

Silicon Drift Detector

The two intermediate layers of the ITS, where the particle density can reach up to 7 tracks/cm^2, consist of Silicon Drift Detectors (SDD). Thanks to the analog readout, it is capable to provide dE/dx information for the PID.

The sensitive area of the detector is split by the central cathode strip in two drift regions. The bias voltage of the cathode is 2.4 kV and generates a parallel drift field. SDD modules are mounted on ladders. There are 14 ladders with 6 modules in layer 3 and 22 ladders with 8 modules in layer 4 in the beam direction. As is shown in Figure 2.5, modules and ladders overlap to ensures full angular coverage. The cooling of SDD is ensured by two independent water circuits and by air flow.

The front-end electronics consists of three modules. PASCAL contains preampli-

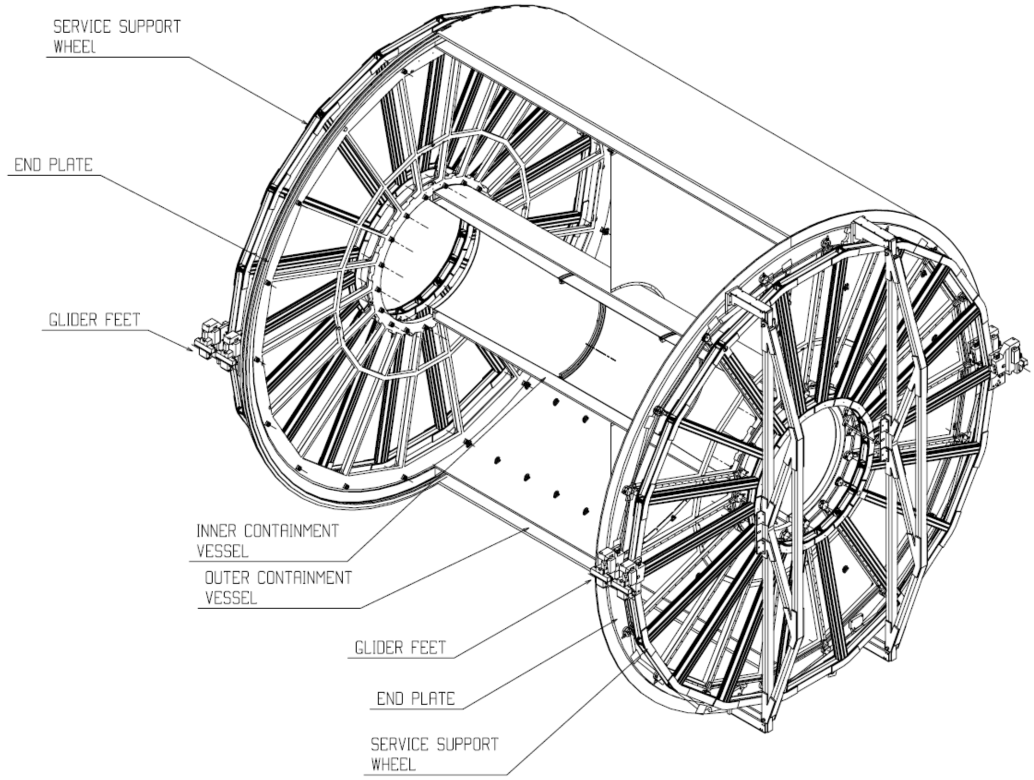

Figure 2.6: A scheme of TPC. Taken from [3].

fier, analog storage and analog to digital converter. The data are then sent to AMBRA, a four-event buffer, which sends data to a zero suppressor and data-compresor CARLOS.

Silicon Strip Detector

The task of the two outer layers of ITS is to match tracks from the TPC. The double sided Silicon Strip Detectors (SSD) provide two dimensional measurement of the track position.

The sensor have 768 strips on each side at an angle of 35 mrad with respect to each other to obtain stereo view. The SSD modules are assembled on ladders of the same type as in the SDD. However, these ladders are up to 25 module-long. The 72 ladders carry 1698 modules and are mounted on Carbon Fibre Composite (CFC) support. As well as in the SDD the ladders are placed so that they overlap. The readout of chips is also analog, so it can be used to obtain the dE/dx information for low-energy particle identification.

2.3.2 TPC

The Time-Projection Chamber (TPC) is the main tracking detector of ALICE. It also provides charged-tracks momentum measurements (from p_T of about 0.1 GeV/c up to 100 GeV/c), particle identification and determination of the primary vertex position.

The TPC has a cylindrical shape with an inner radius of about 85 cm and outer radius of about 250 cm. The overall length in the beam direction is 500 cm. The TPC has full azimuthal coverage. It is divided into 18 sectors as can be seen in Figure 2.6, which results in dead zones for high-momentum particles. As well as in the ITS, the pseudorapidity coverage is $|\eta| < 0.9$, for reduced tracks length up to $|\eta| < 1.5$.

The inner volume is filled with $90\,\mathrm{m}^3$ of mixture of Ne, CO_2 and N_2 and it is divided into two identical parts by a central electrode. The high voltage of 100 kV at the electrode generates an uniform field in the z-axis. Charged particles passing through the volume ionize the gas along their path and create clusters of electrons, which drift with a maximum time of $90\,\mu$s to the end plates.

The necessary amplification and collection of signal is done via multi-wire proportional chambers with pad readout. There are about 560 000 readout pads of different sizes - smaller ($4 \times 7.5\,\mathrm{mm}^2$) located closer to the center, where the track density is higher, and larger ($6 \times 15\,\mathrm{mm}^2$) located far from the center. The readout chambers are normally closed by a gate in the form of grid and the gate is opened by the L1 trigger.

The signal from TPC is preamplified and shaped in PASA modules followed by ALice Tpc ReadOut (ALTRO) chips, which contain an analog to digital converters, a digital processors and a multi-event buffers. If a L2 trigger signal is received, the data are sent by optic cables to the DAQ. Size of an event after zero-suppression and data encoding in case of central Pb-Pb collision is around 90 MB, however the total TPC bandwidth is 27 GB/s, so it is possible to transfer up to 300 central collision per second.

For a precise position calibration, the TPC uses a system of lasers with mirrors inside the volume. The other option is to use cosmic rays, which in the form of muons pass to the underground area making tracks in the chamber.

2.3.3 TOF

The Time-Of-Flight (TOF) detector is designed for particle identification in the intermediate momentum range, below 2.5 GeV/c for pions and kaons and up to 4 GeV/c for protons.

The detector covers a cylindrical surface in the same pseudorapidity range as ITS and TPC ($|\eta| < 0.9$). Its length is 741 cm, the internal radius is 370 cm and the external one is 399 cm. Due to its huge size, it is a gaseous detector based on Multi-gap Resitive-Plate Chamber (MRPC). Ionization produced by a charged particle starts an avalanche. However due to the small distances between chambers, there is no drift time, which results in excellent time resolution of 40 ps.

The TOF front-end electronics is designed for very high time resolution and it is used as a pretrigger for TRD and as a L0 trigger for UPC, minimum bias pp collisions, for barrel detectors calibration and for cosmic-ray physics.

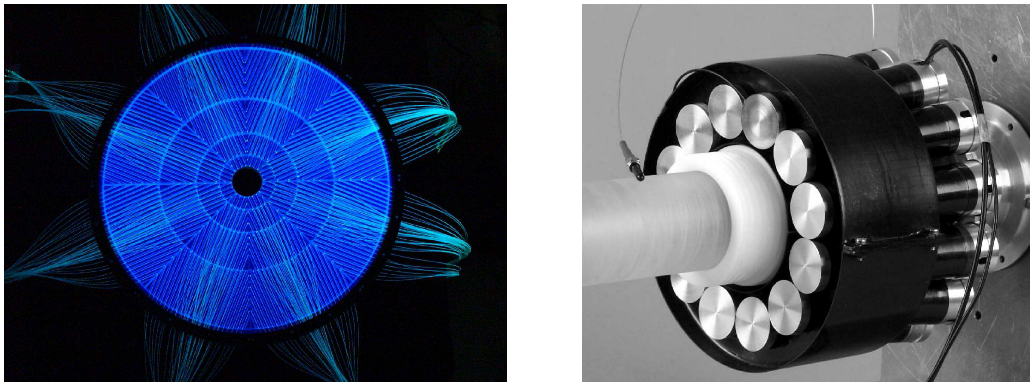

Figure 2.7: V0 and T0 detectors. Taken from [3, 4].

2.3.4 V0

The V0 detectors are a small angle detectors positioned around the beam pipe on each sides of the interaction point. It consist of two arrays of scintillator counters - V0A and V0C covering the pseudorapidity ranges $2.8 < \eta < 5.1$ ($-3.7 < \eta < -1.7$). There are 32 elementary counters in V0A and V0C array arranged in 4 rings as can be seen in Figure 2.7.

The V0 detectors have several important functions. The main task is to provide an on-line L0 centrality trigger and rejection of beam-gas events. The system provides a minimum bias trigger for central barrel detectors and validation of dimuon triggers. V0 play an important role in luminosity measurement.

2.3.5 T0

The T0 detectors consist of two arrays of photomultipliers tubes equipped with Cherenkov radiators (Figure 2.7). The detectors are located on opposite sides of the interaction point covering pseudorapidity range of $4.5 < \eta < 5$ and$-3.3 < \eta < -2.9$. The time resolution is better than 50 ps.

The main task of T0 is to provide fast timing signals for L0 trigger, wake-up signal for TRD and collision time for TOF detector. The precise time is used for confirming the location of the IP with accuracy better than 1.5 cm. The T0 also provide a fast multiplicity evaluation (minimum bias, central and semi-central) and luminosity measurement.

2.3.6 ZDC

The ZDCs are located on both sides of the interaction point (IP) at a distance of 116 m. Each ZDC consists of two detectors - one for protons (ZP) and one for neutrons (ZN). The proton spectators are deflected by LHC magnets outside the beam pipe, so the ZP is placed outside the beam pipe and it is shown at Figure 2.8. The ZN detector is placed between the beam pipes at 0°, because neutrons are not deflected by the magnetic field. The ZDCs can be moved down when not in use to protect them from radiation damage.

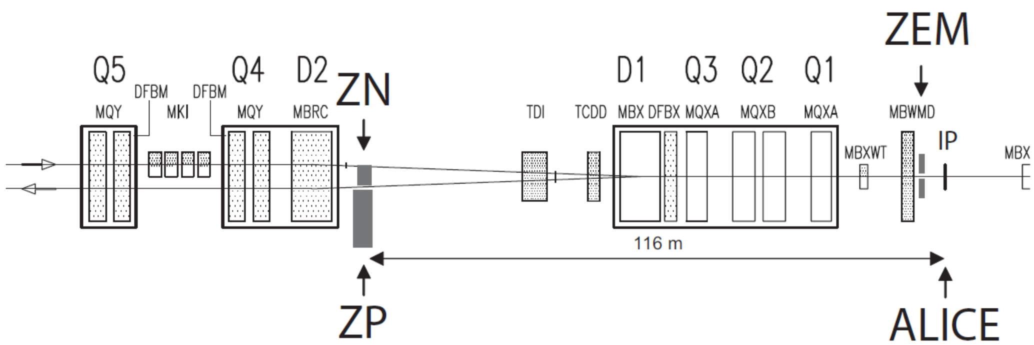

Figure 2.8: The locations of the neutron (ZN), proton (ZP) and electromagnetic (ZEM) calorimeters. Taken from [3].

An incident particle generates a shower in a dense absorber, which is usually called "passive" material. Because there is small amount of space for neutron calorimeter, a very dense tungsten alloy is used as passive material for ZN. For proton calorimeter there is no limit for space, so it is made of brass. The shower produces Cherenkov radiation in quartz fibres, which are used as "active" material. The optical readout is divided into five photomultiplier tubes.

Hadronic calorimeters are complemented by two electromagnetic calorimeters (ZEM), which are placed 7 meters from IP on opposite side of the muon arm (Figure 2.8).

Cherenkov calorimeters provide very fast signal, therefore the ZDCs are used as L1 triggers providing three different centralities (central, semi-central and minimum bias events).

2.4 Trigger system and DAQ

The ALICE Central Trigger Processor (CTP) is designed to select rare events and also common events, which are scaled down to satisfy the bandwidth of the DAQ system, which is 1.25 GB/s [3]. It is also optimized for different running modes such as ion-ion, proton-ion and proton-proton.

The fast part of the trigger is split into two levels. A Level 0 (L0) signal reaches the detectors at 1.2 μs, but it does not contain all trigger inputs. A Level 1 (L1) signal arrives at 6.5 μs and carries the remaining inputs. The final level of the trigger is the Level 2 (L2), which waits for the past-future protection. Then the data produced by detectors are sent through the Detector Data Link (DDL) to the DAQ, where the event builder is located (see Figure 2.9).

2.5 Offline computing

The computing infrastructure is coordinated by the Worldwide LHC Computing Grid (WLCG). All data are recorded in a very large computing centre at CERN called Tier-0. The role of large regional computing centres, called Tier-1, is to provide a safe

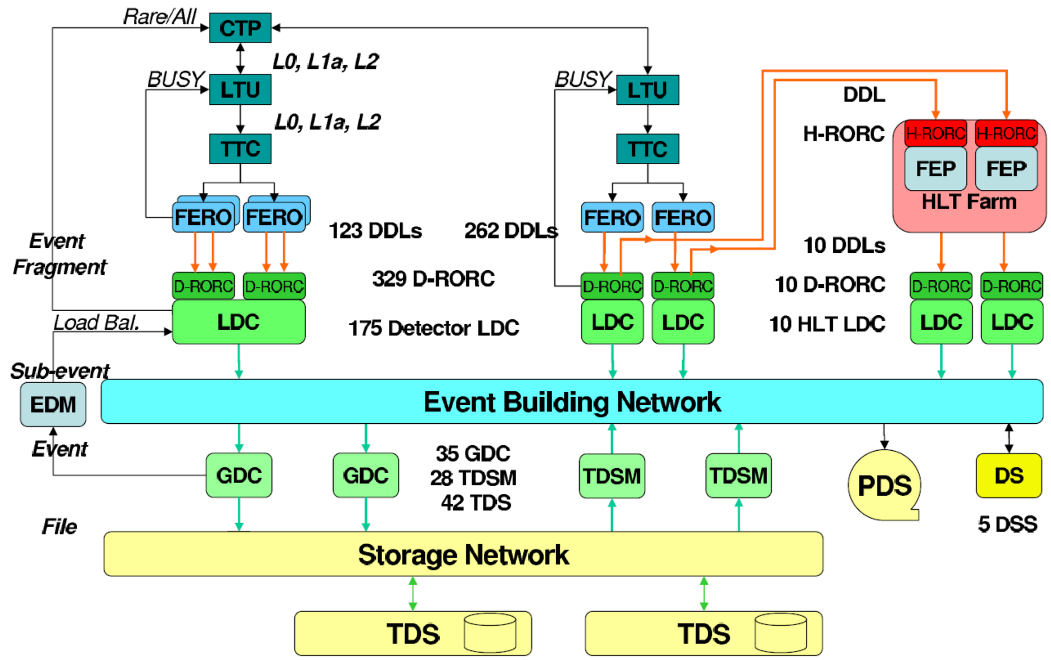

Figure 2.9: An architecture of the ALICE DAQ. Taken from [3].

copy of the data and organised processing. Smaller centres, called Tier-2, are used for simulations and end-user analysis.

2.5.1 Data processing

The data in proton-proton collisions are recorded at an average rate of 100 MB/s [3] into the CERN Tier-0 computing centre, where the first pass processing including recontruction, calibration and alignment takes place. From the Tier-0 centre a copy to the CASTOR tapes and to the Tier-1 centres is done.

During the nucleus-nucleus runs, the rate of data acquisition is so high that the Tier-0 computing capability is insufficient. Therefore the RAW data are copied to CASTOR and partially exported to the Tier-1 centres. The Tier-0 centre provides a rapid feedback to the offline chain. During the shutdown of the accelerator, the data are exported to the Tier-1 centres, then are first time processed.

During the first pass recontruction, high-precision alignment, calibration data, Events Summary Data (ESD) and Analysis Object Data (AOD) are produced. The first pass data are used for improvement of the code for second pass processing. The final data are produced in the third pass.

One full copy of the raw data is stored at CERN Tier-0 centre, the second one is distributed among the Tier-1 centres.

2.5.2 AliRoot

AliRoot [3] is an Object-Oriented framework based on the ROOT system complemented by the AliEn system, which gives access to the computing grid. The AliRoot is used for simulation, alignment, calibration, recontruction, visualisation and analysis of the experimental data. It was designed for maximal re-usability and modularity. For example it is possible to replace well defined part, such as event generator or Monte Carlo with no impact on the rest parts. For the response of the ALICE detector, GEANT3, GEANT4 and FLUKA packages are available.

2.5.3 Reconstruction and analysis

The process of recontruction starts with individual steps for each detector, e.g. cluster finding. Then the primary vertex is reconstructed followed by the track reconstruction and particle identification. Finally the secondary vertices from uncharged particles, cascades and kink decay are found. The output of recontruction is the ESD, which contain information about charged particle tracks, particle identification and information about decays or cascade topology.

Analysis starts from the ESD produced during reconstruction. Afterward AOD are produced with content condensed from the ESD as well as specific physical information like momentum, energy and other. Scheduled analysis is performed via so-called “trains”. These “trains” are sent to the Tier-1 centres, where are processed.

The end-user analysis start from condensed AODs produced in trains and it is designed for local system processing. If greater computing capacity is needed, the data can be submitted as a job to the AliEn system, which distributes the data on Tier-2 or Tier-1 centres.

Chapter 3

Summary of relevant measurements

In this chapter some new measurements of ultra-peripheral collisions at ALICE and measurement of ρ^0 cross-section at HERA collider are discussed.

3.1 ALICE results

In ALICE coherent photoproduction of ρ^0 mesons in ultra-peripheral Pb-Pb collisions were measured. This analysis is very similar to my work and therefore it is described in more detail.

3.1.1 Coherent rho photoproduction in Pb-Pb UPC

In the following text are the results of [5] presented. It was the first measurement at the LHC of coherent photoproduction of ρ^0 mesons in ultra-peripheral Pb-Pb collisions. The data were collected during the 2010 Pb-Pb run at an energy of $\sqrt{s_{NN}} = 2.76\,\text{TeV}$. Two different triggers were used. The former required at least two hits in the TOF detector, the latter required at least two hits in the outer layer of the SPD and no activity in any of the V0 detectors.

Track and event selection

The events had to satisfy following requirements:

1. A primary vertex identified within 10 cm of the nominal IP position along the beam direction.
2. Exactly two tracks reconstructed in the TPC and ITS.
3. Empty V0.
4. The energy loss in the TPC consistent with pions within 4 standard deviations from the Bethe-Bloch parametrization ($\sigma^2_{\pi^+} + \sigma^2_{\pi^-} < 16$).
5. The track pair transverse momentum below $150\,\text{MeV/c}$ and rapidity $|y| < 0.5$.

6. The track pair have tracks of opposite charge.

The track selection required:

1. Each track has at least 70 space points in TPC.
2. χ^2 per degree of freedom better than 4 in TPC.
3. Each track has at least one hit in the SPD with a χ^2 per degree ITS hit less than 36.
4. The distance between the track and the primary vertex less than 2 cm along the beam direction.
5. Less than $0.0182 + 0.035/p_T^{1.01}$ cm (p_T in GeV/c) in the place perpendicular to the beam direction.

Using these requirements the four-momenta of the two tracks are reconstructed. The pair p_T can be seen in Figure 3.1. The coherent peak below 0.15 GeV/c is clearly visible. The distribution is compared with the STARLIGHT prediction. The tail is explained by the incoherent production of ρ^0.

The final sample is corrected for acceptance and efficiency using a flat distribution in invariant mass, rapidity, transverse momentum and azimuthal angle. GEANT3 was used for the propagation of particles through the detector.

The mass distribution (Figure 3.2) was parametrized by the Söding formula and also by the Ross-Stodolsky function. The visible peak at 1.3 GeV was explained by the production of $f_2\,(1270)$, which also decays into $\pi^+\pi^-$ pair.

In Figure 3.3 can be seen the obtained cross section in mid-rapidity compared with predictions of several models. The ALICE data are consistent with STARLIGHT and GM models.

The total cross section as a function of $\sqrt{s_{NN}}$ is shown in Figure 3.4. The results from ALICE and STAR are compared with the STARLIGHT and GDL predictions. Both results are in a good agreement with a STARLIGHT prediction.

3.2 HERA results

The photon-proton interactions were studied by the H1 and ZEUS collaboration at HERA electron-proton collider.

3.2.1 H1 Collaboration results

The following text is based on the "Elastic Photoproduction of ρ^0 Mesons at HERA" [6] article published by H1 Collaboration.

The elastic ρ^0 photoproduction cross section was study at total energies, $W_{\gamma p} = 55$ and 187 GeV, of the gamma-proton centre-of-mass system. Almost real photons radiated along the electron beam (26.7 GeV electrons in 1993 and 27.5 GeV in 1994) interact with 820 GeV protons. The two measurements were made under very different experimental conditions. In the low $W_{\gamma p}$ analysis, the ρ^0 rest frame was boosted

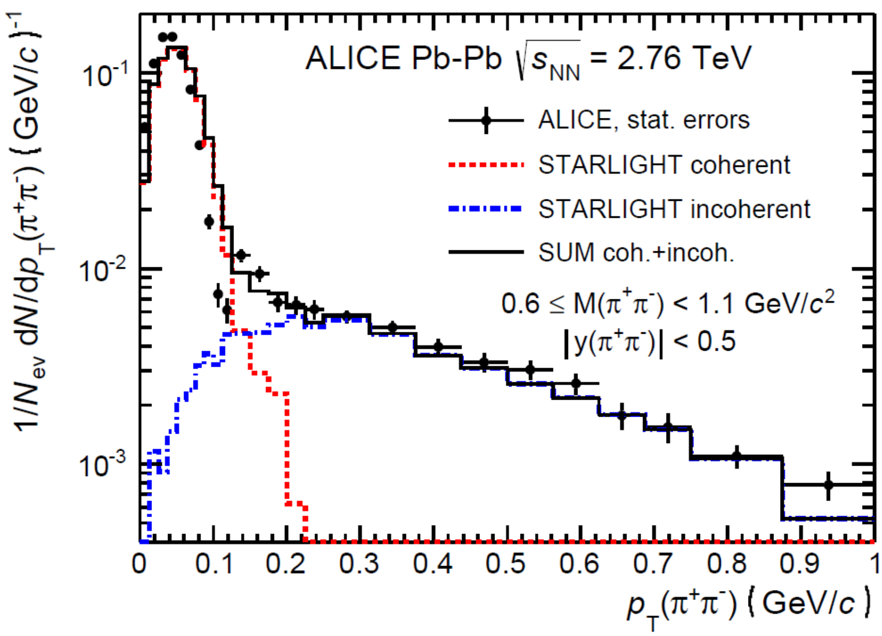

Figure 3.1: Transverse momentum distribution for $\pi^+\pi^-$ pairs. The red and blue histograms shows the normalized p_T distribution from STARLIGHT. Taken from [5].

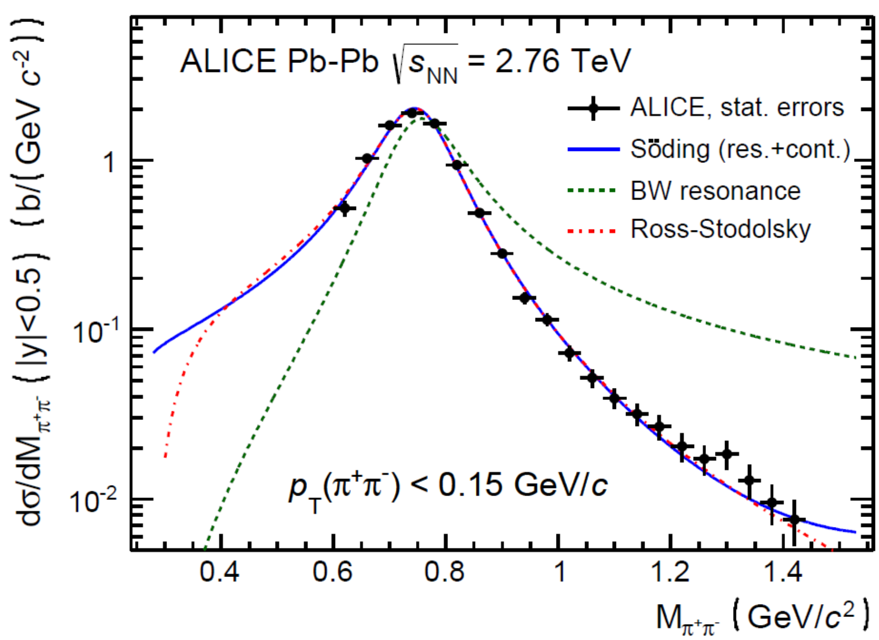

Figure 3.2: Invariant mass distribution for pions corrected for acceptance and efficiency. The blue curve corresponds to a Söding parametrization fit, red shows the Ross-Stodolsky parametrization. Taken from [5].

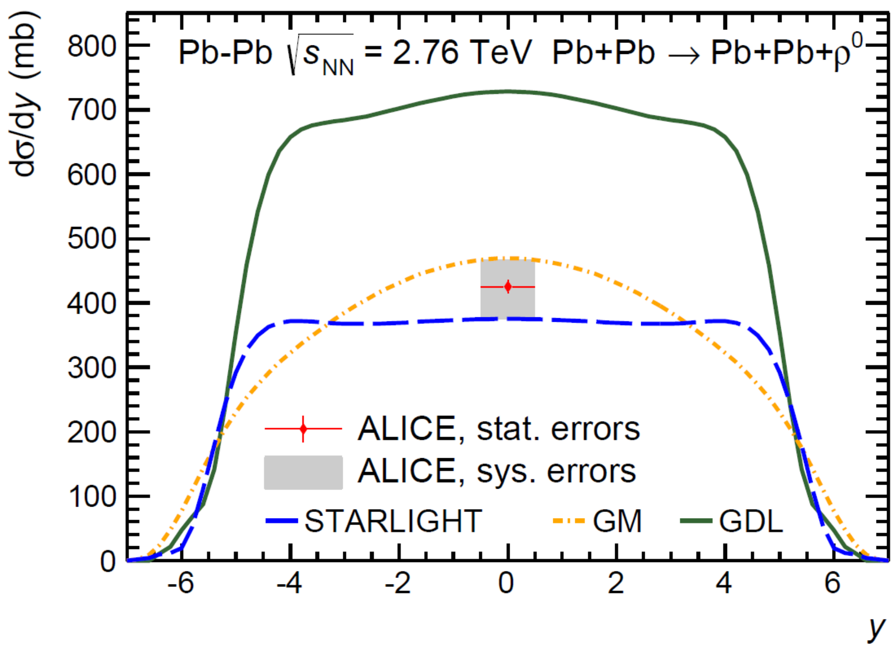

Figure 3.3: The cross section $d\sigma/dy$ for three models compared with the ALICE results. Taken from [5].

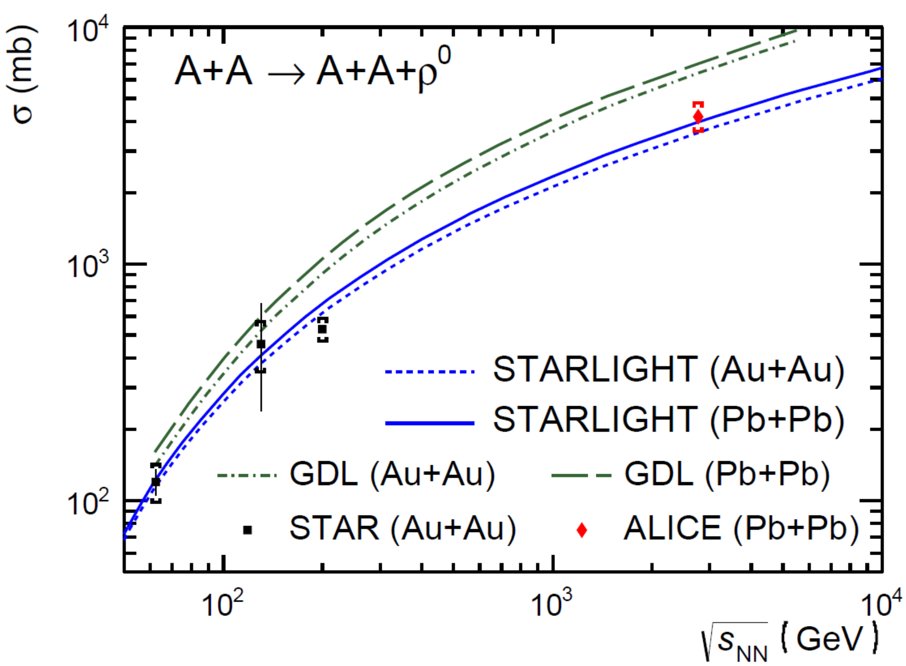

Figure 3.4: The results from ALICE and STAR compared with the STARLIGHT and GDL predictions. Taken from [5].

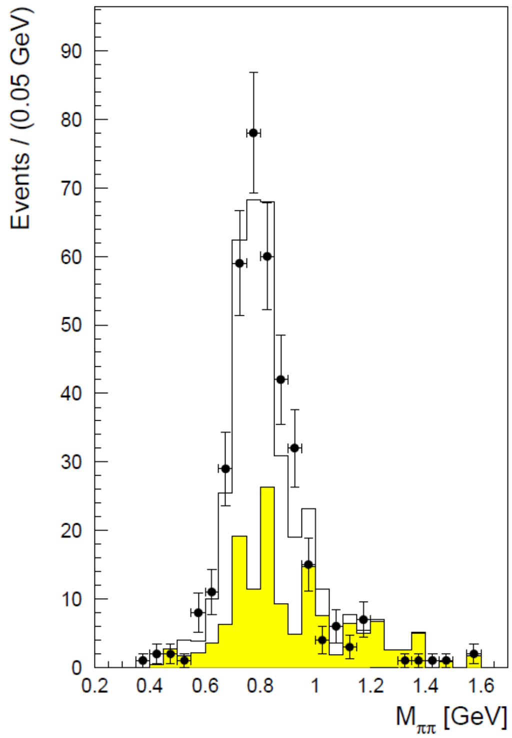

Figure 3.5: Reconstructed $M_{\pi\pi}$ distribution for the low $W_{\gamma p}$ data at HERA. Taken from [6].

by about 1 unit of rapidity toward the electron beam direction. The decay products were observed in the central tracking (H1) detector. The reconstructed $M_{\pi\pi}$ distribution can be seen in Figure 3.5.

At higher $W_{\gamma p}$ analysis, the ρ^0 rest frame was boosted by about 3 units of rapidity toward the electron beam direction. The decay products were outside the acceptance region of the tracking detector, thus a reconstruction of the hadronic final state in the calorimeters was necessary. However, it results in a worse spatial and energy resolution.

The results of measurements of H1 collaboration can be seen in Figure 3.6. The cross section for the elastic photoproduction of ρ^0 mesons was $\sigma\left(\gamma p \to \rho^0 p\right) = 9.1 \pm 0.9\,(\text{stat.}) \pm 2.5(\text{syst.})$ μb at $\langle W_{\gamma p}\rangle = 55$ GeV and $\sigma\left(\gamma p \to \rho^0 p\right) = 13.6 \pm 0.8\,(\text{stat.}) \pm 2.4(\text{syst.})$ μb at $\langle W_{\gamma p}\rangle = 187$ GeV for $2M_\pi < M_{\pi\pi} < M_\rho + 5\mathit{\Gamma}_\rho$, where M_π is the mass of pion, $M_{\pi\pi}$ is the invariant mass of the pion pair, M_ρ is the mass of ρ^0 and $\mathit{\Gamma}_\rho$ is its decay width.

3.2.2 ZEUS Collaboration results

Elastic and proton-dissociative production of ρ^0 has been studied by the ZEUS Collaboration at HERA for photon-proton centre-of-mass energies in the range $50 < W_{\gamma p} < 100\,\text{GeV}$ and for $|t| < 0.5$ GeV^2, where t is the square of the transferred four-momentum [7].

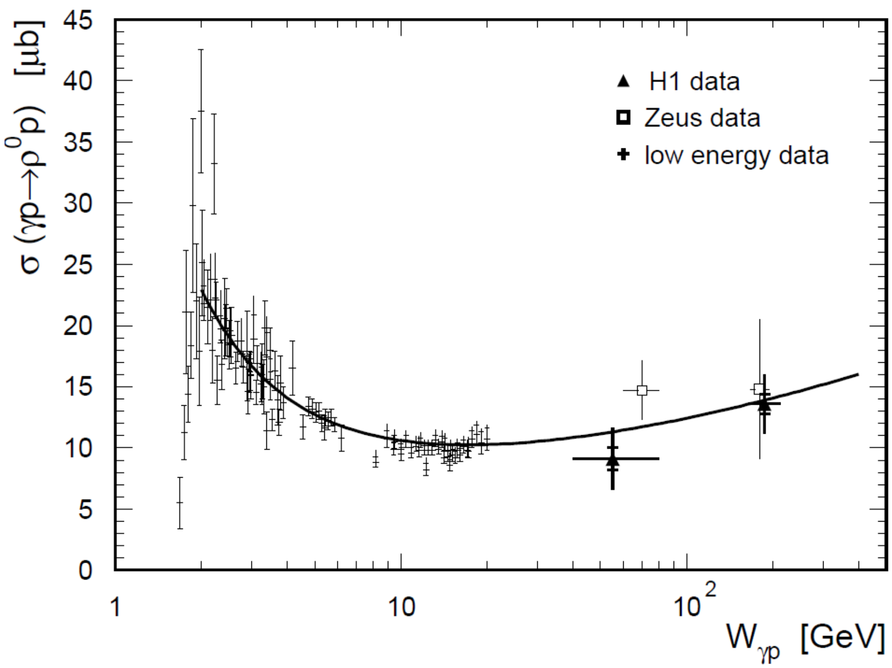

Figure 3.6: The dependence of the elastic ρ^0 photoproduction cross section including old measurements and prediction based on a VMD model. Taken from [6].

The integrated cross section was determined in four $W_{\gamma p}$ bins. The results of HERA measurements are summarized in Table 3.1. In Figure 3.7 are shown results of measurements from HERA and VMD model and Pomeron predictions.

$\langle$W$\rangle$ [GeV]	$\sigma_{\gamma p \to \rho^0 p}$ [μb]
55	10.9 ± 0.2 (stat.)$^{+1.5}_{-1.3}$ (syst.)
65	10.8 ± 0.2 (stat.)$^{+1.3}_{-1.1}$ (syst.)
75	11.4 ± 0.3 (stat.)$^{+1.0}_{-1.2}$ (syst.)
90	11.7 ± 0.3 (stat.)$^{+1.1}_{-1.3}$ (syst.)

Table 3.1: Elastic ρ^0 photoproduction cross section in four $W_{\gamma p}$ bins measured by HERA. Taken from [7].

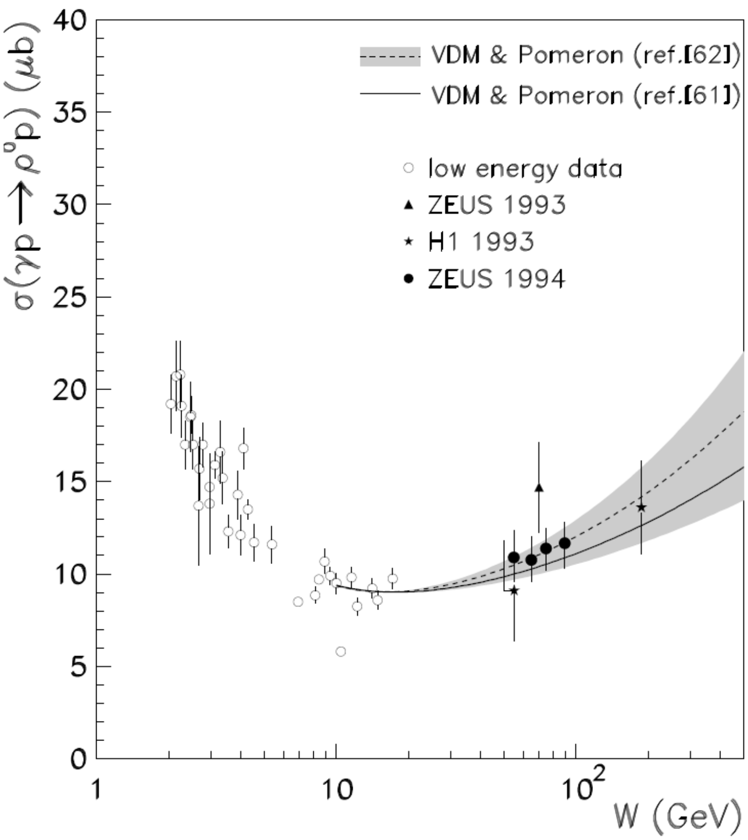

Figure 3.7: The integrated cross section as a function of the centre-of-mass energy $W_{\gamma p}$. Taken from [7].

Chapter 4

Rho analysis in p-Pb UPC at ALICE

This chapter presents results of my work. It is a first measurement of exclusive ρ^0 production in p-Pb UPC. A chapter starts with the describing of the data sample. Then a quality assurance of data is shown. The chapter continues with information about computing luminosity, selection criteria and the difficulties in background subtraction. After that a Monte Carlo data, which are used for estimation of efficiency and acceptance of the detector, are described. Finally a computed cross section of ρ^0 is presented and it is compared to the HERA results.

4.1 Data used

In this thesis p-Pb data collected in 2013 (LHC13b period) at $\sqrt{s_{NN}} = 5.02\,\text{TeV}$ are used. These data can be found here:

/alice/cern.ch/user/a/alitrain/PWGUD/UD_pPb_AOD/36_20150123-1133/merge.

This analysis use the following 5 runs:

Runs: 195344, 195346, 195351, 159389, 195391.

These data were triggered by the CINT1 trigger. This trigger asks, if there is an activity in SPD or in V0A or in V0C. For producing the AOD data the AOD154 version was used.

The AOD data contains events, which satisfy criteria similar to the Pb-Pb analysis at ALICE [5]. The number of reconstructed tracks is exactly two and following track selection are required:

1. Each track has at least 70 space points in TPC.
2. χ^2 per degree of freedom better than 4 in TPC.
3. Each track has at least one hit in the SPD with a χ^2 per degree ITS hit less than 36.
4. The distance between the track and the primary vertex less than 2 cm along the beam direction.

5. Less than $0.0182 + 0.035/p_T^{1.01}$ cm (p_T in GeV/c) in the place perpendicular to the beam direction.

These data contain 101744 events.

4.2 Data quality assurance

Before analyzing data sample it is necessary to check all variables in each run. Because it is good to automatize this for further study, a macro to cheack variables related to track, vertex position and so on was made. The positive and negative tracks were performed separately. The idea is to compare the distribution of data in each run to the distribution from all runs. If there is no problem both distribution should similar. So the ratio in each run to the average of all runs should be consistent with one. If not, it is important to know about it and understand it. In Figure 4.1 an example of this QA for azimuthal distribution is shown.

The QA procedure allowed to discover that the data from one run (195390) was not ok. The strange behavior can be seen in Figure 4.2, where the number of TPC clusters in this run is shown. As can be seen in this plot, the shape of the TPC clusters distribution looks different from other runs. Upon further investigation this agreed with what the experts wrote in the Run Condition Table (RCT). The data from this run was not considered for further analysis.

4.3 Luminosity

According to Equation 1.2 luminosity is necessary to computing the cross section. The luminosity of the sample can be computed using the C0TVX trigger. The luminosity is then number of triggered events, divided by the cross section of a corresponding trigger:

$$L = \frac{C0TVX}{\sigma_{C0TVX}}. \tag{4.1}$$

The cross section of the C0TVX trigger was already measured by the van de Meer scans and determined as $\sigma_{C0TVX} = (1.59 \pm 0.06)$ b. This result was published in [14]. Two correction for pile-up must be applied to this formula. The first one is caused by more than 1 interaction in one bunch crossing and it can be expressed as:

$$\frac{\mu}{1 - \exp(-\mu)}, \tag{4.2}$$

where μ is a the probability of a pile-up.

The second correction is because of hadron interaction and it can be expressed as:

$$\exp\left(-\mu\frac{CINT1}{C0TVX}\right), \tag{4.3}$$

where CINT1 is the number of events triggered by the CINT1 trigger in analyzed sample.

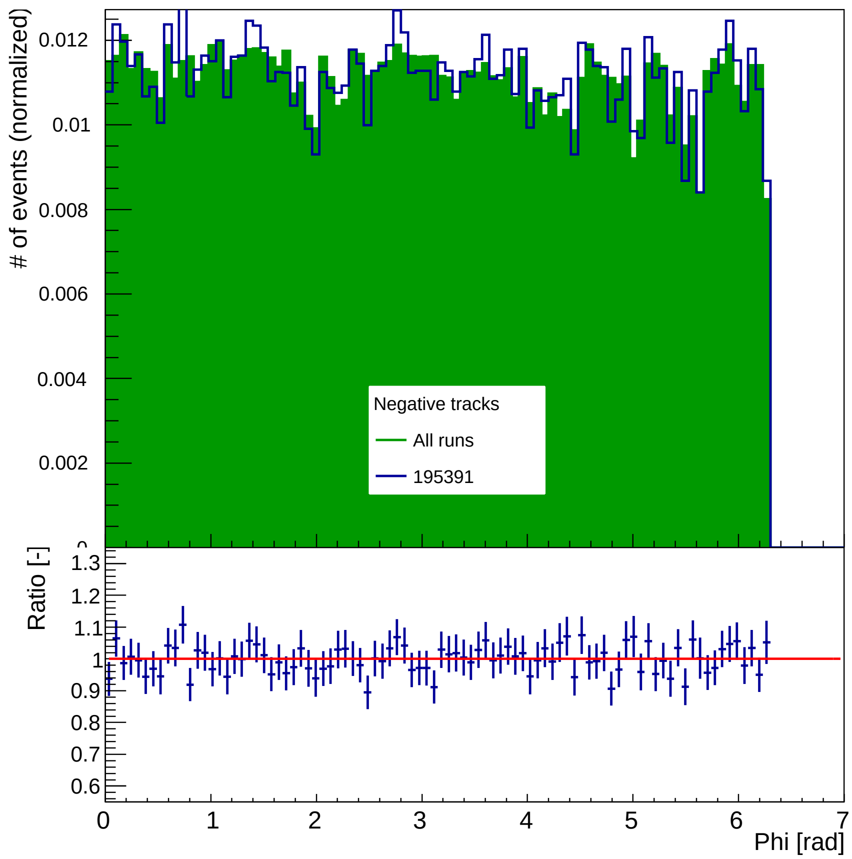

Figure 4.1: An example of the QA - Azimuthal distribution of events for one run compared to the average of all runs.

The whole formula is then following:

$$L = \frac{C0TVX}{\sigma_{C0TVX}} \frac{\mu}{1 - \exp(-\mu)} \exp\left(-\mu \frac{CINT1}{C0TVX}\right). \tag{4.4}$$

All variables for this equation and the computed luminosity are summarized in Table 4.1. The total luminosity of the sample is 1.36 inverse microbarn.

4.4 Global selection criteria

The data satisfy all track selection criteria described in Section 4.1. The events had to satisfy also following requirements:

1. Empty both V0A and V0C.
2. The energy loss in the TPC consistent with pions within 4 standard deviations from the Bethe-Bloch parametrization ($\sigma^2_{\pi^+} + \sigma^2_{\pi^-} < 4^2$).
3. Tracks have an opposite charge.

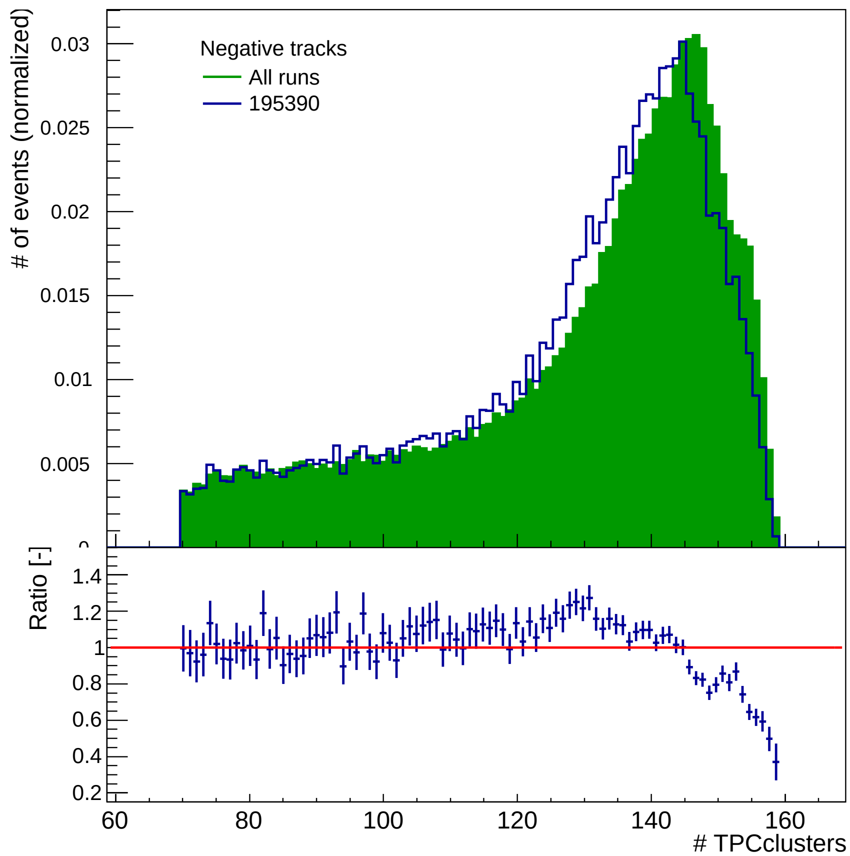

Figure 4.2: A problem discovered by the QA - number of TPC clusters in run 195390 compared to the average of all runs.

4. The distance between primary vertex and vertex from SPD (if exist) is smaller than 2.5 cm.

5. The rapidity of the pion pair is in the range from -0.5 to 0.5.

6. The invariant mass of the pion pair is in the range from 0.6 to 1.3 GeV/c^2.

7. The transverse momentum of the pion pair is less than 0.7 GeV/c.

Table 4.2 summarizes all cuts, which are used and also an resulting number of events after each of these cuts.

4.4.1 V0 decision

This cut is usually called the V0 Veto. Figure 4.3 shows a two-dimensional plot of the V0A and V0C decisions. The explanation of numbers on axis is the following:

3 - Fake signal.

2 - Signal in time, which is not consistent with interaction time and the origin of these events is in the beam-gas interactions.

Run	C0TVX	CINT1	μ	$L\,[\mathrm{mb}^{-1}]$
195344	93079	198857	0,03947	55 ± 2
195346	315864	680340	0,03688	187 ± 7
195351	383679	828885	0,03293	228 ± 9
195389	630341	1415660	0,00896	390 ± 15
195391	808969	1811440	0,00940	501 ± 19
total				1361 ± 51

Table 4.1: Computed luminosity L for each run. C0TVX and CINT1 are numbers of triggered events and μ is the probability of a pile-up.

Selection criteria	Number of events
All data	101744
1	4232
2	4017
3	3568
4	3543
5	2461
6	1857
7	1650

Table 4.2: Number of events after each selection criteria.

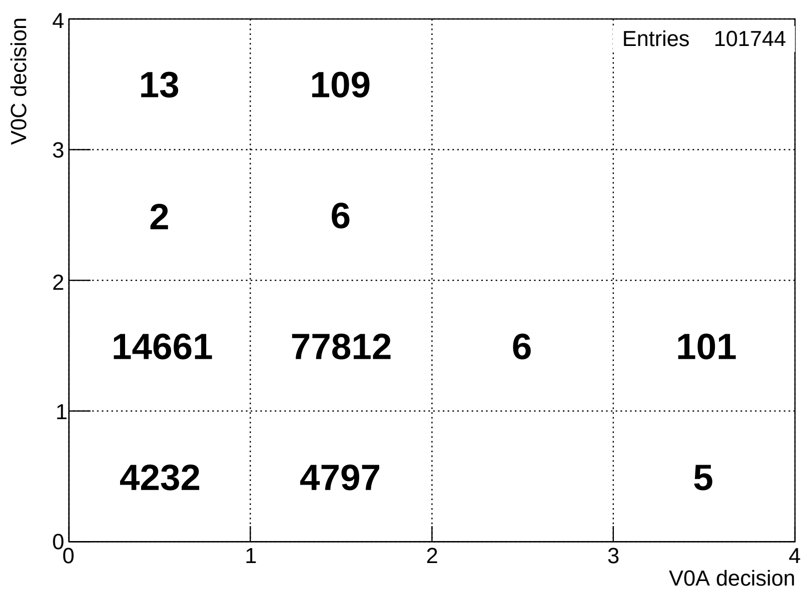

Figure 4.3: V0A decision vs the V0C decision.

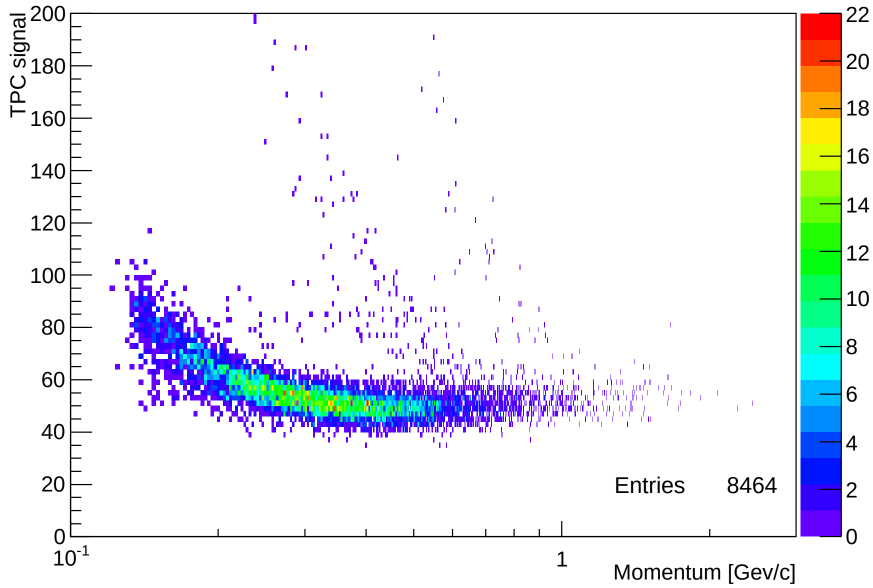

Figure 4.4: Signal in TPC depending on track momentum before the PID cut. Small contamination from kaons, protons and electron is visible.

1 - Signal corresponds with the bunch-crossing time, it means there are tracks in forward rapidities, this is mostly background in this analysis.

0 - No signal in the V0 detector.

Events with zero signal in both V0A and V0C are useful for further analysis. There can not be another tracks in the exclusive production of ρ^0. From 101744 events only 4232 of them survive this cut.

4.4.2 Particle identification

Only tracks which are identified as pions are consistent with a decay of ρ^0 meson. The particle identification is done using the specific ionization lossing dE/dx in the TPC. Pions at low momentum can be easily identified. Figure 4.4 shows the dE/dx TPC signal depending on the track momentum before the cut. Small contamination from kaons, protons and electrons is visible far away from the pions. Events satisfying following equation were considered in further analysis:

$$\sigma_1^2 + \sigma_2^2 < 4^2, \tag{4.5}$$

where σ_1 and σ_2 are mean-square deviations of the first and second track from the Bethe-Bloch expectation in the TPC (Figure 4.6). As can be seen in Figure 4.7 this cut keeps tracks inside the circle with a radius smaller than 4 sigma. The dE/dx signal in the TPC after this cut can be seen in Figure 4.5.

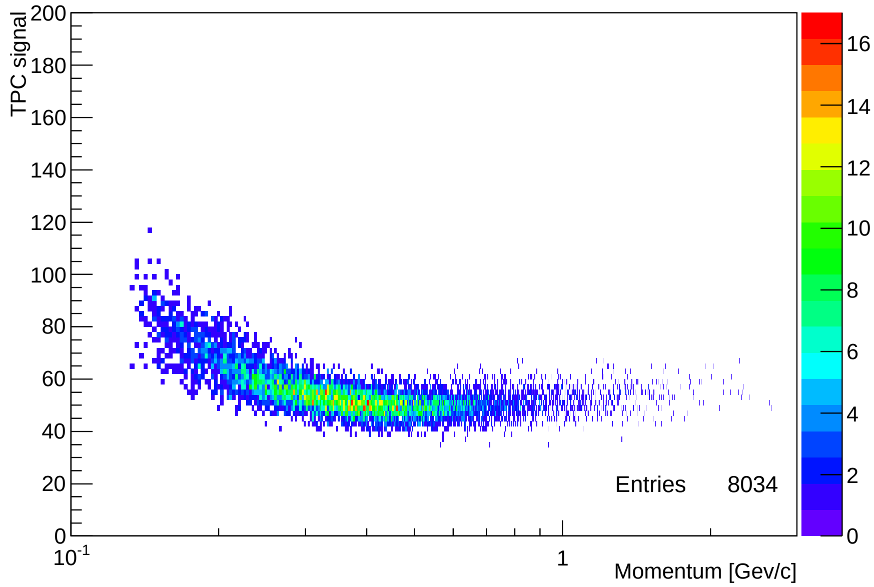

Figure 4.5: Signal in TPC depending on track momentum after the PID cut.

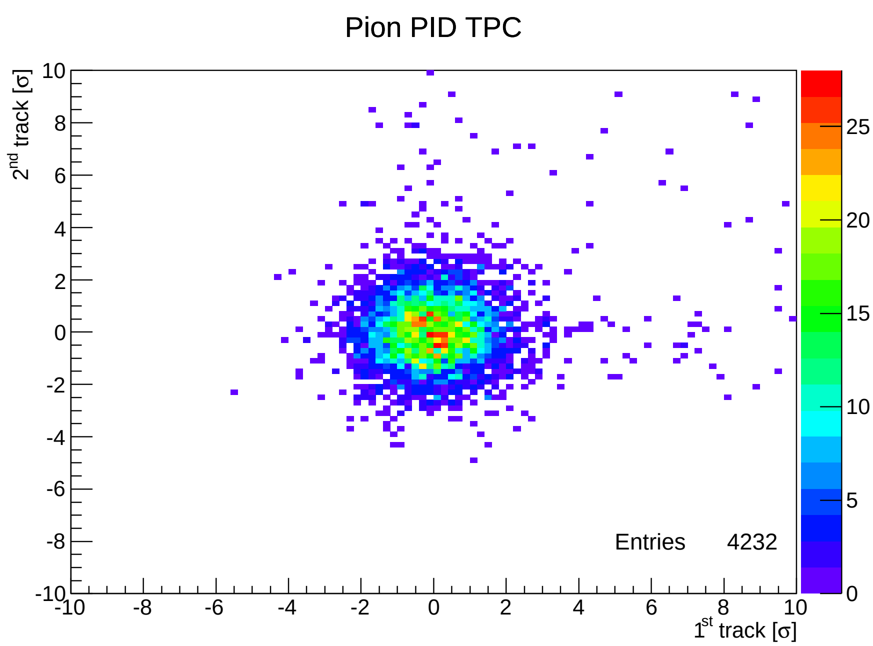

Figure 4.6: 2-dimensional plot of the track distance from an ideal fit before the PID cut.

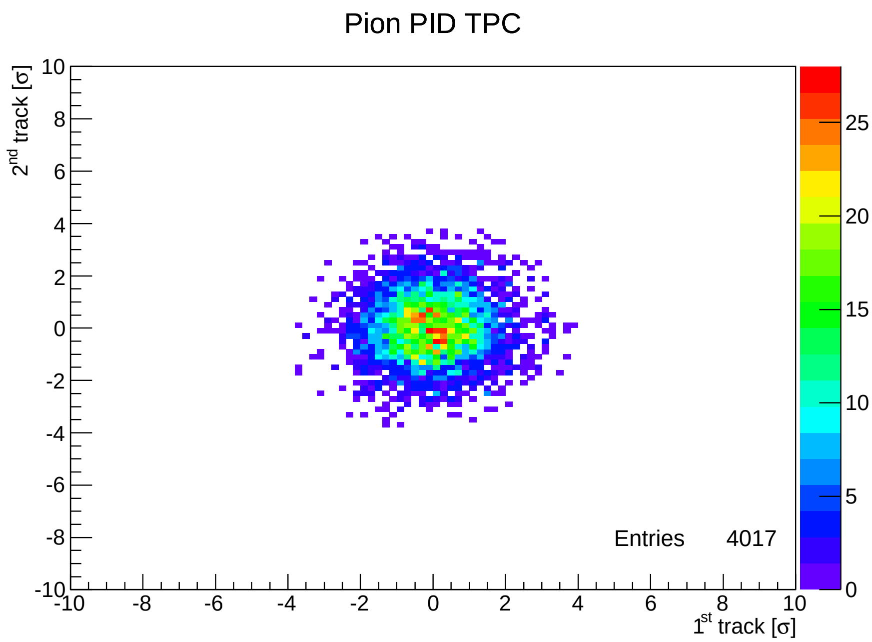

Figure 4.7: 2-dimensional plot of the track distance from an ideal fit after the PID cut.

4.4.3 Opposite charge of tracks

The ρ^0 meson decays into $\pi^+\pi^-$ pair, so both tracks must have opposite charge. Events with the same charge are called the like-sign events. In the like-sign event some of the charge is missing. It means that in these events are particles, which were not reconstructed, for example they were heading into the dead regions of the detector. The importance of like-sign events will be discussed later. In Figure 4.8 can be seen a distribution of charge in my data. As can be seen the contamination from like-sign events is slightly above 10%.

4.4.4 Track cut

Because the TPC readout is slow, some of the reconstructed tracks can be from previous events. To estimate contamination from these events, the SPD vertex can be used. The SPD readout is much faster, so the primary vertex reconstructed by it is correct and the track vertex will be shifted in z-axis. According to [15] I am using events, which have the difference between the SPD and the track vertex in z-axis less than 2.5 cm. However, due to the low multiplicity in UPC, the SPD vertex is not always reconstructed. Therefore, this cut can be used only for events which has the SPD vertex (number contributors larger than 0). In Figure 4.9 is shown the distance between the SPD and track vertex for events. A small contamination from previous events is visible, however, this contamination is smaller than 1%. The same distribution after the cut can be seen in Figure 4.10.

Figure 4.8: Distribution of the charge of tracks.

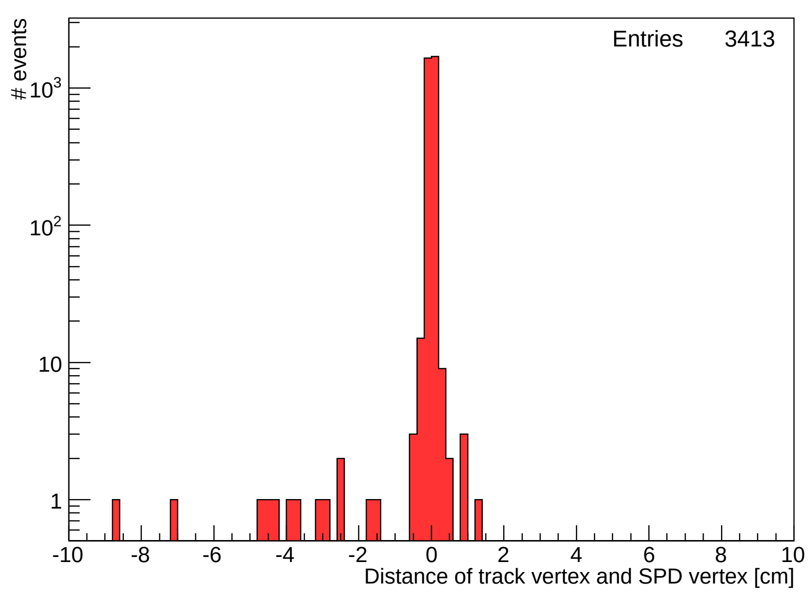

Figure 4.9: The distance between SPD and track vertex before the cut. Small contamination from previous events is visible.

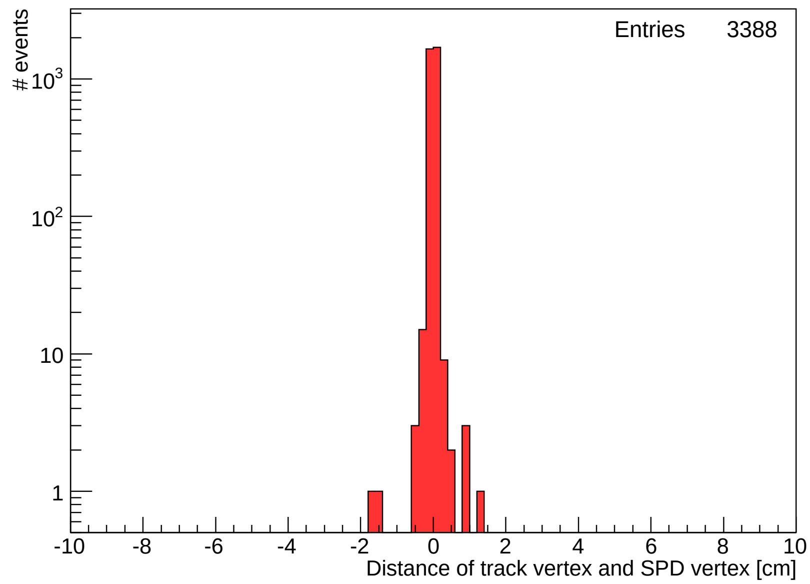

Figure 4.10: The distance between SPD and track vertex after the cut.

4.4.5 Rapidity of the sample

The distribution of the final sample can be seen in Figure 4.11. The rapidity y of sample was chosen in the range from -0.5 to 0.5, where the highest statistics is expected. According to equation [16]:

$$W_{\gamma p}^2 = 2E_p M_\rho \exp(-y), \tag{4.6}$$

where E_p is the energy of a proton and M_ρ is the mass of the ρ^0, the centre-of-mass energy can be computed as $W_{\gamma p} = 88\,\mathrm{GeV}$.

4.4.6 p_T distribution

The transverse momentum of the final sample is shown in Figure 4.12. The p_T was chosen in the range from 0 to 0.7 GeV/c. This range corresponds to the $|t| < 0.5$ GeV^2 that was measured by HERA.

4.4.7 Mass distribution

The distribution of the invariant mass for the selected events is shown in Figure 4.13. The mass distribution is selected around the mass of ρ^0 (between 0.6 and 1.3 GeV).

4.5 Possible other cut

One another possible selection criteria is to identified secondary vertices from weak decays. The position of the primary vertex in x and y axis can be used. This

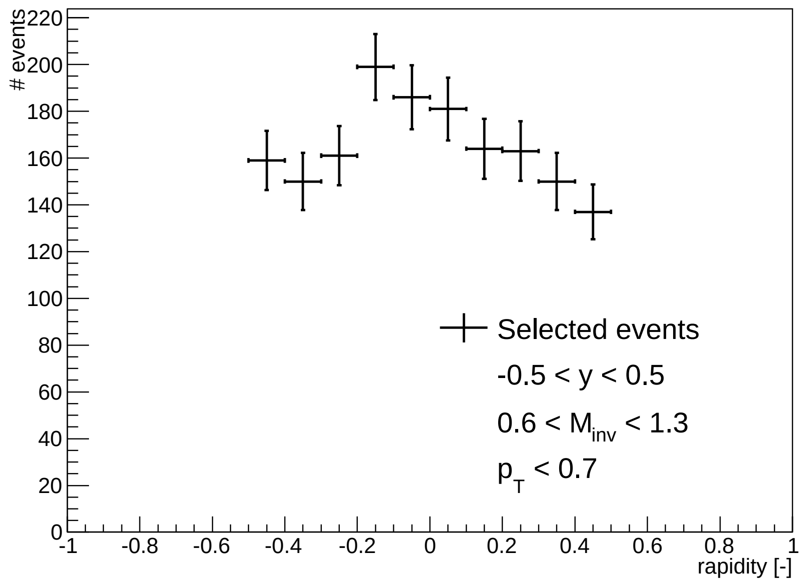

Figure 4.11: Rapidity distribution of the final sample.

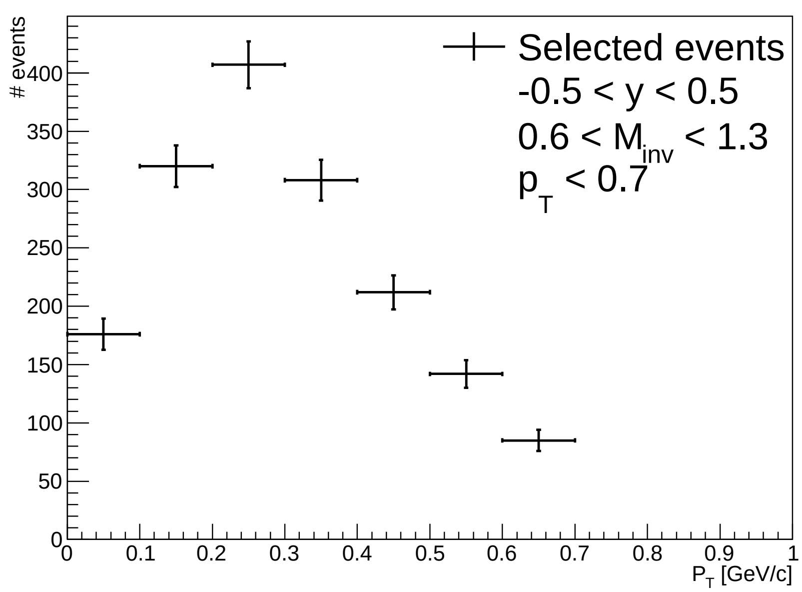

Figure 4.12: Transverse momentum distribution of the final sample.

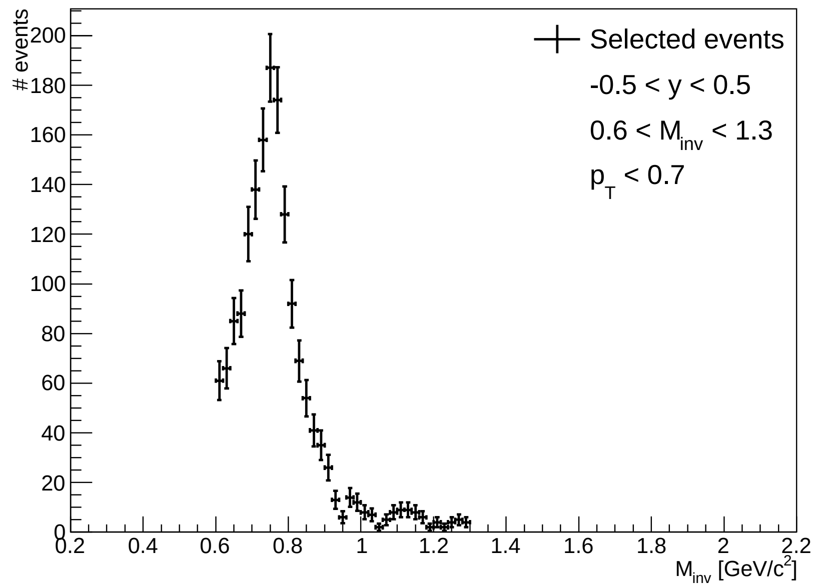

Figure 4.13: Invariant mass distribution of the final sample.

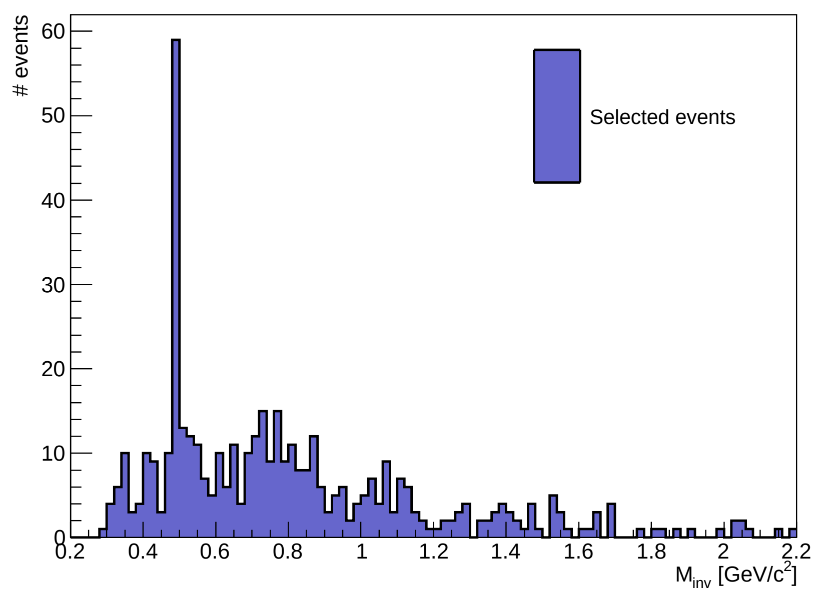

Figure 4.14: Invariant mass distribution with a K0-short peak.

sample	ZDCA energy	ZDCC energy	number of events
A1	< 10	all	1557
B1	< 10	> 10	318
C1	> 10	< 10	59
D1	> 10	> 10	34

Table 4.3: Number of events for different ZDC information for unlike-sign events.

distribution looks like a Gaussian distribution, but there are vertices, which are far away from the average interaction point in each run. These are from weak decays.

In Figure 4.14 is shown the invariant mass distribution of events, which has a primary vertex far away than 0.06 mm from the centre of all vertices in x and y axis. This criteria was used together with unlike-sign events and pion identification. As can be seen a peak at 0.5 GeV is visible. This peak comes from a K0-short particle, which decays weakly with a mean lifetime $\tau \cong 9 \times 10^{-11}$ s.

This results is quite surprising, because K0-short is a strange particle and there are only two reconstructed tracks in my data. One K0-short can not be produced exclusively in UPC, because strangeness quantum number would not be conserved. It showed that there is some background, but this background can be identified and rejected. However, the contamination from K0-short in the final data sample is less than 0.1 % and thus this selection criteria is not considered in this analysis.

4.6 Background

There are several types of a background in data passed through the global selection criteria and track criteria. There are events, which had originally four tracks, but only two were reconstructed as well as in the like-sign events. The number of these events is the same as in the like-sign case and thus it can subtracted from the sample. There is also background from peripheral hadronic collisions and the proton-dissociative background.

To estimate the portion of background, four samples using the information from ZDC were produced. The ZDCA is located in the lead direction and ZDCC in the proton direction. I am using only the neutron ZDCs and threshold 10 in energy.

The overview of four samples can be seen in Table 4.3. The sample A1 corresponds to the events, which have no signal in the lead direction. Sample B1 has signal in proton direction calorimeter and have not signal in lead direction. These are proton-dissociative or hadronic events. The sample C1 stands for events, which has signal only in lead direction. Events in this sample has a hadronic origin, but ZDCC (proton direction) do not see this due to the lower efficiency. Sample D1 left energy in both calorimeters. These events are from hadronic collisions.

Similar samples were produced for the like-sign events as can be seen in Table 4.4. From the unlike-sign samples the like-sign events were subtracted to remove background from four-tracks events. The number of events in final samples can be seen in Table 4.5.

I suppose that the efficiency of ZDCA for hadronic process is very high (close to

sample	ZDCA energy	ZDCC energy	number of events
A2	< 10	all	92
B2	< 10	> 10	37
C2	> 10	< 10	14
D2	> 10	> 10	8

Table 4.4: Number of events for different ZDC information for like-sign events.

sample	ZDCA energy	ZDCC energy	number of events
A	< 10	all	1465
B	< 10	> 10	281
C	> 10	< 10	45
D	> 10	> 10	26

Table 4.5: Number of events for different ZDC information for subtracted like-sign events.

the 1). Then sample A contains only elastic and dissociative production of ρ^0 and sample B contains only dissociative production of ρ^0. To estimate the number of dissociative events in sample A, it is necessary to know efficiency of the ZDCC. The efficiency of the ZDCC for hadronic process can be easily computed from samples C and D as:

$$\varepsilon_{ZDCC}^{hadron} = \frac{D}{D+C}. \tag{4.7}$$

Now I assume that this efficiency is similar to the efficiency of ZDCC for dissociative production. Then the dissociative events can estimate as: $\frac{B}{\varepsilon_{ZDCC}^{hadron}}$ and subtracted bin by bin from sample A. After this, sample A should contains only elastic events.

4.7 Monte Carlo data

To estimate acceptance and efficiency a Monte Carlo data are used. These data are the official MC data and they are available on the following link:

https://alice.its.cern.ch/jira/browse/ALIROOT-5903.

The used generator is AliGenStarlight (STARLIGHT integrated into aliroot). The number of generated events was 20,000 in each run. From these data a AOD tree was produced in the same way as my data. For the ALICE detector response a GEANT3 model of ALICE in STARLIGHT was used.

A quality assurance of these data was done in the same way as in the real data mentioned above.

4.8 Efficiency and acceptance

The acceptance and efficiency is computed as the ratio of events, which passed through the same selection criteria, and events, which were generated. The gen-

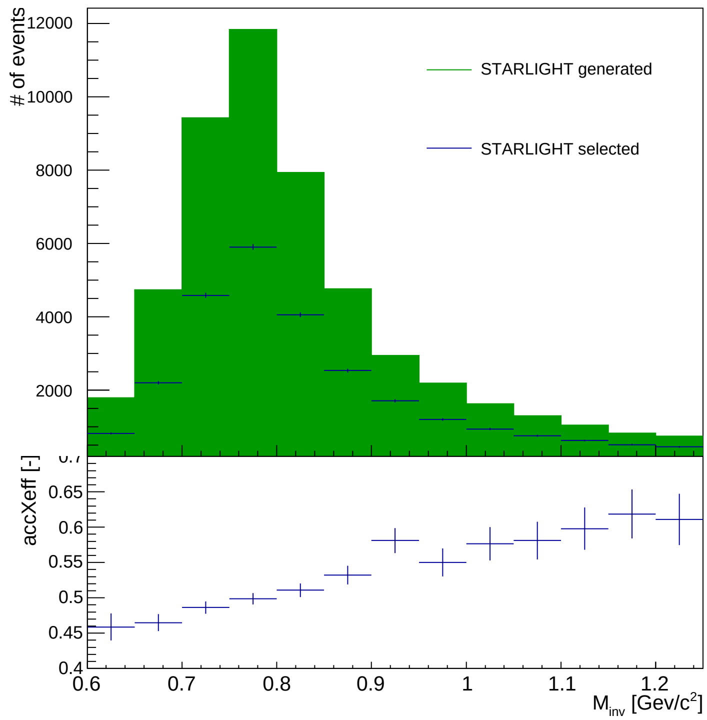

Figure 4.15: Acceptance × efficiency for invariant mass distribution.

erated events are also preselected to respect the same kinematic variables, namely rapidity from -0.5 to 0.5, $p_T < 0.7\,\text{GeV}$ and invariant mass in the range from 0.6 to 1.3 GeV.

The acceptance and efficiency was computed in each bin for invariant mass, p_T and rapidity distribution. The error was computed only from events, passed through the analysis, the error of generated events was not considered.

The final plot of generated, selected events and their ratio can be seen on following figures - 4.15, 4.16, 4.17.

The final sample was divided by this acceptance and efficiency in each bin.

4.9 Cross section estimation

The number of candidates can be estimated from the invariant mass distribution. The invariant mass of $\pi^+\pi^-$ pair has not a Breit-Wigner shape due to the pion resonance. This shape can be described by the Söding formula [15]:

$$\frac{d\sigma}{dm_{\pi\pi}} = |A \cdot BW(m_{\pi\pi}, m_{\rho^0}, \Gamma(m_{\pi\pi})) + B|^2, \tag{4.8}$$

with the relativistic Breit-Wigner function:

$$BW(m_{\pi\pi}, m_{\rho^0}, \Gamma(m_{\pi\pi})) = \frac{\sqrt{m_{\pi\pi} m_{\rho^0} \Gamma(m_{\pi\pi})}}{m_{\pi\pi}^2 - m_{\rho^0}^2 + i m_{\rho^0} \Gamma(m_{\pi\pi})} \tag{4.9}$$

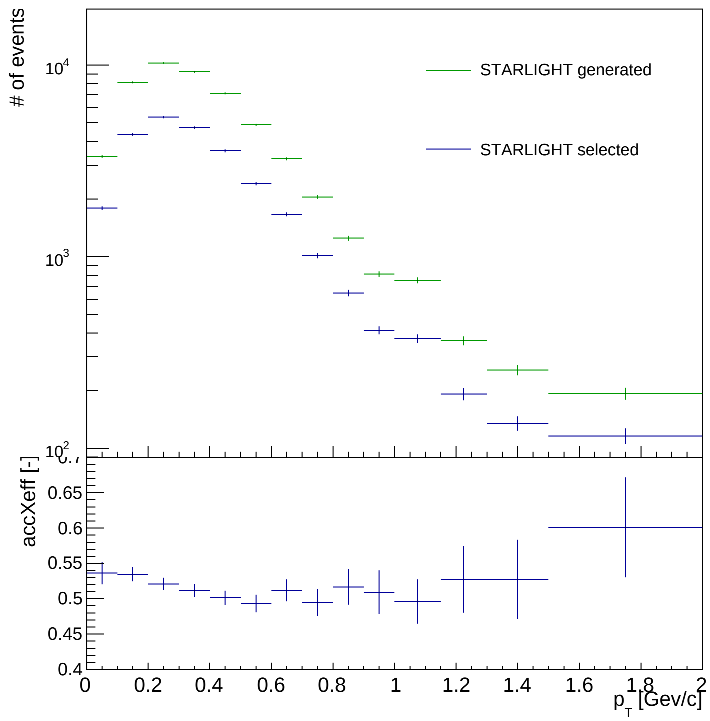

Figure 4.16: Acceptance $\times$ efficiency for p_T distribution.

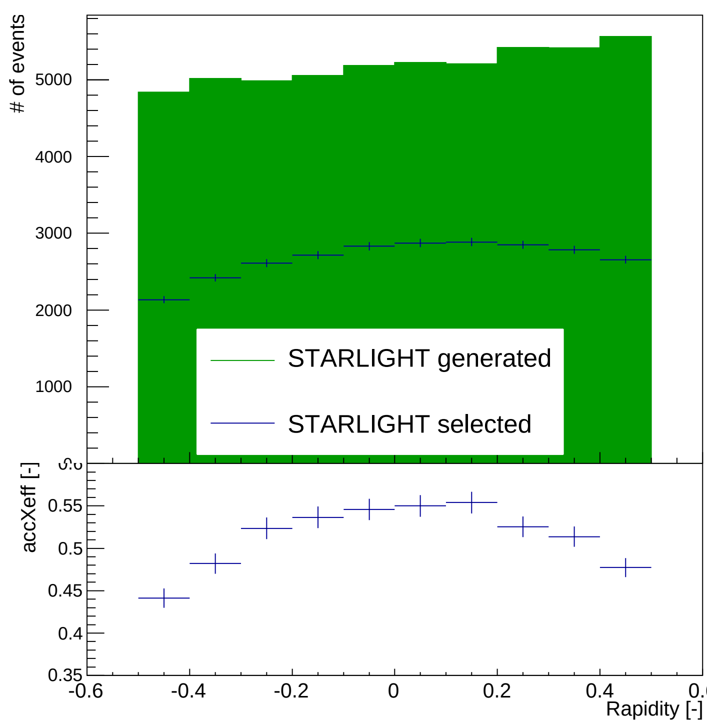

Figure 4.17: Acceptance $\times$ efficiency for rapidity distribution.

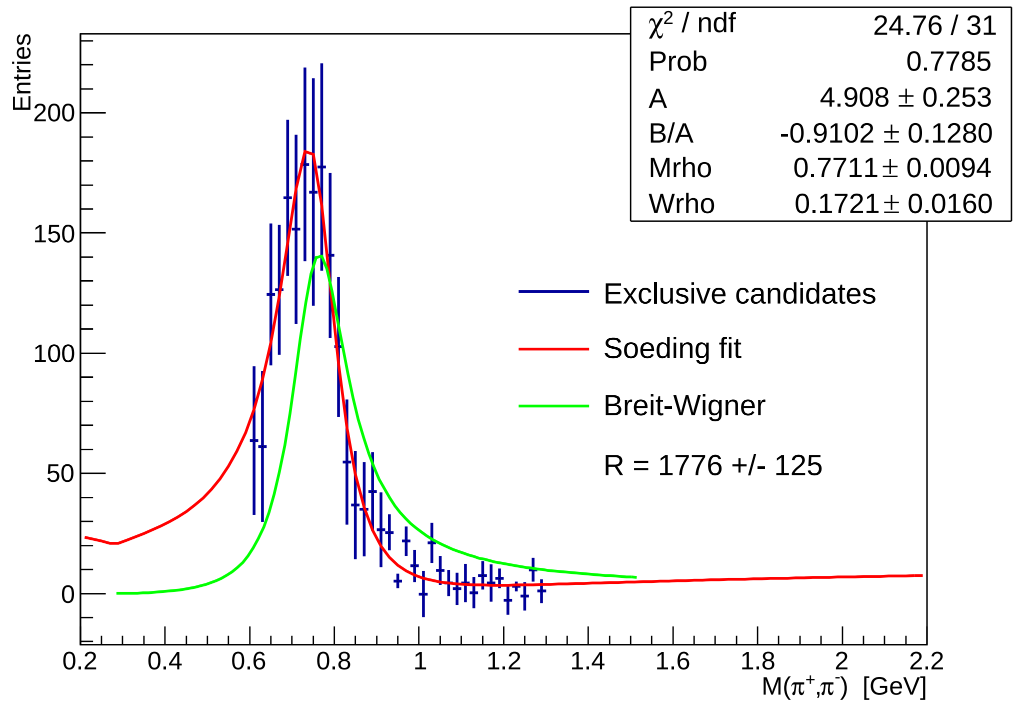

Figure 4.18: The invariant mass distribution with the Söding fit and with the Breit-Wigner part. R is the number of obtained candidates.

and mass-dependent width:

$$\Gamma(m_{\pi\pi}) = \Gamma_{\rho^0} \frac{m_{\rho^0}}{m_{\pi\pi}} \left(\frac{m_{\pi\pi}^2 - 4m_\pi^2}{m_{\rho^0}^2 - 4m_\pi^2} \right)^{\frac{3}{2}}. \tag{4.10}$$

B is the non-resonant amplitude and it is a real number. The four parameters (A,B,Γ_{ρ^0},m_{ρ^0}) are determined by a fit.

The data was fitted by a Söding formula as can be seen in Figure 4.18. The mass of the ρ^0 determined from the fit is compatible with a PDG value [12].

The number of candidates is obtained by an integration of the Breit-Wigner part in the range of from $2M_\pi < M_{\pi\pi} < M_{\rho^0} + 5\Gamma_{\rho^0}$, where M_π is the mass of pion and $M_{\pi\pi}$ is the invariant mass of the pion pair. The estimated number of candidates R from the Söding fit is:

$$R = 1778 \pm 125.$$

The proton-lead differential cross section is given by:

$$\frac{d\sigma}{dy} = \frac{R}{L \cdot \Delta y \cdot BR}, \tag{4.11}$$

where L is the total luminosity of the sample obtained in Section 4.3, Δy is the width of the rapidity bin and BR is branching ratio. In my case $L = (1361 \pm 51)\,\mathrm{mb}^{-1}$, $\Delta y = 1$ and $BR = 1$. The computed cross section is then

$$\frac{\mathrm{d}\sigma}{\mathrm{d}y} = 1.31 \pm 0.09\,(\mathrm{stat.}) \pm 0.05(\mathrm{syst.})\ \mathrm{mb}.$$

The systematic error is computed only from the systematic error of luminosity.

According the Equation 1.8 this result can be transformed to the photon-proton cross section. The photon flux of the lead was computed as $N_{\gamma/Pb} = 112$ using Equation 1.10. The photon-proton cross section is then

$$\sigma = 11.65 \pm 0.83\,(\mathrm{stat.}) \pm 0.44(\mathrm{syst.})\ \mu\mathrm{b}.$$

This is a result for the centre-of-mass energy $W_{\gamma p} = 88\,\mathrm{GeV}$ and it is in agreement with HERA results presented in Section 3.2.

4.10 Discussion of future measurement

Next steps of this analysis will be the study of the background subtraction, precise computing of all systematic uncertainties, measurement of the $|t|$ dependence and its comparison to HERA results. Then the same analysis will be done using a CCUP2 sample, which contains around 50 times higher statistics. Using this sample a higher centre-of-mass energy in range that was not measured at any experiment before can be studied.

Summary

The aim of this work was to compute preliminary cross section for exclusive photoproduction of a ρ^0 meson in ultra-peripheral p-Pb collisions. This process was never measured at the LHC before.

I presented here the ultra-peripheral collisions and their relationship to the photoproduction with an especially focus on photoproduction of a ρ^0 meson, which was studied in this work. I described ALICE detector at LHC and its subdetectors used in this analysis. The relevant measurements at HERA accelerator and at ALICE were also presented.

In this thesis have been performed following activities. Quality assurance of the obtained data sample was done. A strange behavior in one run was found. The data from this run was not considered for further analysis. Second, the luminosity of this sample was computed including corrections for pile-up. Next a selection criteria were established and deeply studied. K0-short was found in this data set. One K0-short can not be produced exclusively in UPC, because strangeness quantum number would not be conserved, and it originates from the background.

To estimate the remaining background in the sample a new procedure was proposed. This procedure uses the fact that ALICE has ZDC neutron calorimeters and they offer the possibility to tag hadronic and dissociative background. Using these background sample and some assumptions, the background remaining in the sample can be subtracted. The results obtained with this procedure are compatible with previous measurements at HERA, but the validity of the assumptions has not yet been studied in detail. The acceptance and efficiency of ALICE detector was estimate using STARLIGHT Monte Carlo data. From the obtained number of candidates and luminosity a preliminary p-Pb cross section for exclusive production of ρ^0 was found to be:

$$\frac{d\sigma}{dy} = 1.31 \pm 0.09\,(\text{stat.}) \pm 0.05\,(\text{syst.})\ \text{mb}.$$

This cross section was converted to the photon-proton cross section at the centre-of-mass energy $W_{\gamma p} = 88\,\text{GeV}$:

$$\sigma = 11.65 \pm 0.83\,(\text{stat.}) \pm 0.44\,(\text{syst.})\ \mu\text{b},$$

which is in agreement with HERA results presented in Section 3.2.

The progress of this work is regularly presented at the UPC meetings of the ALICE Collaboration. Next steps of this analysis will be the study of the background subtraction, precise computing of all systematic uncertainties, measurement of the $|t|$ dependence and its comparison to HERA results. Then the same analysis will be done using a CCUP2 sample, which contains around 50 times higher statistics. Using this sample a higher centre-of-mass energy in range that was not measured at any experiment before can be studied. This results will be presented to the ALICE Collaboration to be submitted, as a research article of the Collaboration, to an internal refereed journal.

Bibliography

[1] M. Schott and M. Dunford, "Review of single vector boson production in pp collisions at $\sqrt{s} = 7$ TeV," *Eur.Phys.J.*, vol. C74, p. 2916, 2014.

[2] CERN, "BIG SCIENCE The LHC in pictures," https://bigscience.web.cern.ch/bigscience/en/lhc/lhc2.html, [online 1.4.2015].

[3] The ALICE Collaboration and others, *The ALICE experiment at the CERN LHC*. Institute of Physics Publishing and SISSA, 2008.

[4] ALICE Collaboration, "ALICE Technical Design Report on Forward Detectors: FMD, T0 and V0," CERN, Tech. Rep., 2004.

[5] J. Adam *et al.*, "Coherent ρ^0 photoproduction in ultra-peripheral Pb–Pb collisions at $\sqrt{s_{\mathrm{NN}}} = 2.76$ TeV," 2015.

[6] S. Aid *et al.*, "Elastic photoproduction of rho0 mesons at HERA," *Nucl.Phys.*, vol. B463, pp. 3–32, 1996.

[7] ZEUS Collaboration. (1997) Elastic and Proton-Dissociative ρ^0 Photoproduction at HERA. arXiv:hep-ex/9712020v1.

[8] C. A. Bertulani, S. R. Klein, and J. Nystrand, "Physics of ultra-peripheral nuclear collisions," *Ann.Rev.Nucl.Part.Sci.*, vol. 55, pp. 271–310, 2005.

[9] J. Contreras and J. Tapia Takaki, "Ultra-peripheral heavy-ion collisions at the LHC," *Int.J.Mod.Phys.*, vol. A30, no. 08, p. 1542012, 2015.

[10] M. Benayoun, H. B. O'Connell, and A. G. Williams, "Vector meson dominance and the ρ meson," *Phys.Rev.*, vol. D59, p. 074020, 1999.

[11] S. R. Klein and J. Nystrand, "Exclusive vector meson production in relativistic heavy ion collisions," *PHYSICAL REVIEW C*, vol. 60, p. 014903, 1999.

[12] K. Olive *et al.*, "Review of Particle Physics," *Chin.Phys.*, vol. C38, p. 090001, 2014.

[13] CERN, "About CERN," http://home.web.cern.ch/about, [online 28.2.2015].

[14] B. B. Abelev *et al.*, "Measurement of visible cross sections in proton-lead collisions at $\sqrt{s_{\mathrm{NN}}} = 5.02$ TeV in van der Meer scans with the ALICE detector," *JINST*, vol. 9, no. 11, p. P11003, 2014.

[15] C. Mayer, "Coherent Photo-Production of ρ^0 Vector-Mesons and of e^+e^- pairs in Ultra-peripheral Pb-Pb Collisions at $\sqrt{s_{NN}} = 2.76$ TeV," *ALICE Internal Notes*, 2014.

[16] A. Baltz, G. Baur, D. d'Enterria, L. Frankfurt, F. Gelis *et al.*, "The Physics of Ultraperipheral Collisions at the LHC," *Phys.Rept.*, vol. 458, pp. 1–171, 2008.